uS

FACULTY OF SCIENCE AND TECHNOLOGY

MASTER'S THESIS

Study programme / specialisation: Master of Science in Mathematics and Physics / Physics	The *spring* semester, *2023* Open
Author: Zaryab Ahmed (268142)	
Supervisor at UiS: Alex B. Nielsen Co-supervisor: External supervisor(s): Jose M. Ezquiaga	
Thesis title: Modified Kerr and Black Hole Ringdown	
Credits (ECTS): 60	
Keywords: GR , Gravity, Black Holes, Gravitational Waves, LIGO, Kerr, QNM spectrum	Pages: 62 + appendix: 4 Stavanger, (15th June 2023)

ZARYAB AHMED

DEPARTMENT OF MATHEMATICS AND PHYSICS

Modified Kerr and Black Hole Ringdowns

Master's Thesis - - June 2023

I, **Zaryab Ahmed**, declare that this thesis titled, "Modified Kerr and Black Hole Ringdowns" and the work presented in it are my own. I confirm that:

- This work was done wholly or mainly while in candidature for a master's degree at the University of Stavanger.

- Where I have consulted the published work of others, this is always clearly attributed.

- Where I have quoted from the work of others, the source is always given. With the exception of such quotations, this thesis is entirely my own work.

- I have acknowledged all main sources of help.

Abstract

In the post-merger phase of a black hole binary system, the remnant object is a perturbed black hole emitting gravitational radiation in the form of Gravitational Waves (quasi-normal modes) before admitting a stable state. Observations of gravitational waves can thus be used to test and constrain deviations from Einstein's theory of gravity. The no-hair theorem says that only 2 parameters are required to characterize an astrophysical black hole described by the Kerr metric; mass and spin. However, in the post-Kerr approximation, the metric incorporates non-Kerr parameters. We assume that the observed ringdown can be described by the Johanssen-Psaltis metric and use LIGO data to constrain the deviation parameter. Compared to existing constraints, our analysis finds a tighter constraint on the deviation parameter ϵ_3 using GW190521 ringdown data.

Acknowledgements

Contents

Chapter 1

Introduction

1.1 Einstein's Field Equations

One of the profound findings of the 20th century is the establishment of General Relativity by Albert Einstein where he connects space and time into one object and describes the universe in this new picture. His interpretation of the universe is based on the interplay of spacetime curvature and matter within it, given by the famous Einstein's Field Equations (EFE):

$$R_{\mu\nu} - \frac{1}{2}Rg_{\mu\nu} = \frac{8\pi G}{c^4}T_{\mu\nu} \tag{1.1}$$

The quantity $g_{\mu\nu}$ is the metric tensor that describes the spacetime, the quantities $R_{\mu\nu}$ and R are the Ricci Curvature Tensor and the Ricci scalar, respectively, built out of the spacetime metric $g_{\mu\nu}$, $T_{\mu\nu}$ encodes information about the distribution of matter in the spacetime, G is the universal gravitational constant, c is the speed of light, π is the mathematical constant and 8 is an integer. EFE are nonlinear partial differential equations in $g_{\mu\nu}$.

Depending on the complexity of the spacetime, the components of the metric can be different. To describe Minkowski (flat) spacetime in cartesian coordinates we use the metric:

$$\eta_{\mu\nu} = \begin{bmatrix} -1 & 0 & 0 & 0 \\ 0 & 1 & 0 & 0 \\ 0 & 0 & 1 & 0 \\ 0 & 0 & 0 & 1 \end{bmatrix} \tag{1.2}$$

Since we are now dealing with (3,1), three space and one time, dimensional space-time, we need a 4-vector to address the information associated with a particle. So instead of just using vectors of the form $[x, y, z]$, we will be using 4-vectors of the form $[t, x, y, z]$ to properly denote the position, velocity, momentum etc of the particle. In cartesian coordinates, the position of a particle would look like this:

$$x^\alpha = (t, x, y, z) \text{ and } x_\alpha = g_{\alpha\beta} x^\beta \tag{1.3}$$

Where the upstairs and downstairs index is used to differentiate between contravariant and covariant vectors, respectively. One can transform between these two kinds of vectors with the appropriate use of the metric tensor (upstairs to downstairs) and the inverse of the metric tensor (downstairs to upstairs). Considering the simple example of flat spacetime metric tensor $\eta_{\mu\nu}$ the transformations shown above are performed as

$$\eta_{\alpha\beta} x^\beta = \begin{bmatrix} -1 & 0 & 0 & 0 \\ 0 & 1 & 0 & 0 \\ 0 & 0 & 1 & 0 \\ 0 & 0 & 0 & 1 \end{bmatrix} * [t, x, y, z] = [-t, x, y, z] = x_\alpha \tag{1.4}$$

Throughout this text, we set $G = c = 1$ and adopt the metric signature to be $(-1, 1, 1, 1)$. The vacuum solutions, where $T_{\mu\nu} = 0$, mentioned here are black holes and Boyer-Lindquist coordinates (t, r, θ, ϕ) are used to write out the metric that describes a black hole, as the reader will see in the coming sections. These are singularities of the spacetime and have many interesting physical properties. We will be going through one of these, the light ring structure which is caused by photons/gravitons orbiting the black hole at a radial location $r = r_{ph}$. This phenomenon was observed for Sagitarius A* which is to-date the best image we have of a black hole and also, proof of their existence.
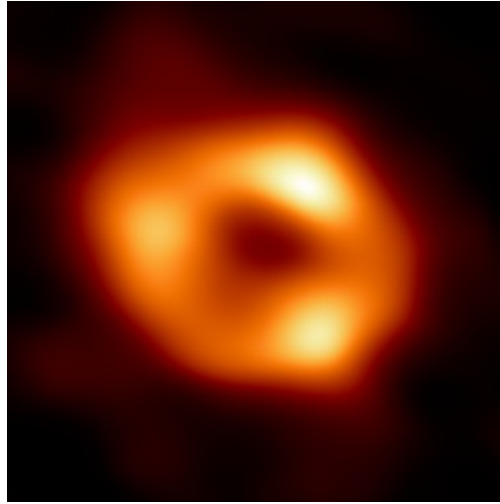
Figure 1.1: First ever image of a black hole, Sagitarius A*, produced by the Event Horizon Telescope.[1]

1.2 Gravitational Waves

Gravitational waves (GW) are 'ripples' in space-time caused by some of the most violent and energetic processes in the Universe. Einstein predicted the existence of gravitational waves in 1916 in his general theory of relativity. Einstein's mathematics showed that massive accelerating objects (things like neutron stars or black holes orbiting each other) would disrupt space-time in such a way that 'waves' of undulating space-time would propagate in all directions away from the source. These cosmic ripples would travel at the speed of light, carrying with them information about their origins, as well as clues to the nature of gravity itself[2].

There are multiple expected types of gravitational waves like continuous, burst, stochastic and compact binary inspiral[2]. Continuous ones are produced by a rotating massive object such as a neutron star due to imperfections in its geometric structure. Stochastic ones are small waves travelling in every direction in the the universe and and randomly mixed together. They are expected to originate at the Big Bang. Bursts are random occurrences of a signal where the origin of the signal is unknown. Lastly, we have compact binary inspiral. We are interested in gravitational waves produced by the compact binary inspiral which are a consequence of two massive objects spiralling toward each other and finally colliding.

The entire process is referred to as a 'Compact Binary Coalescence' where the two compact objects can either be two black holes or a black hole and a neutron star or a pair of neutron stars. More precisely, we focus of the port-merger phase of the coalescence of two black holes where the progenitors have merged into a single object which is an unstable black hole emitting gravitational radiation as it stabilizes (ringdown). These are the GWs observed by LIGO at the Livingston and Hanford detectors. All detected signals are catalogued by LIGO and can be found in open-access documents called 'Gravitational Wave Transient Catalogue'. There are 3 catalogues currently available which contain the observations made in three runs; O1, O2 and O3. A fourth run, O4, is currently active and LIGO is recording data as you read this document. Detected signals are a completely new window into the universe and currently one of the major research fields in physics. One of the major objectives is to test GR with observational data.

The observed GW signal has two polarizations, due to polar and axial tensor perturbation :

$$h_+ + \iota h_\times = \frac{M}{r} \sum_{lmn} A_{lmn} e^{\iota(\omega_{lmn}t + \phi_{lmn})} e^{-t/\tau_{lmn}} S_{lmn} \tag{1.5}$$

This might be a scary expression but the reader is advised to keep calm as there is more discussion about it in the following sections. The objects of interest in the above equation are ω_{lmn} and τ_{lmn}, the orbital frequency and damping time. The other parameters are irrelevant for our purpose since they mainly describe the sky location and the distance of the event.
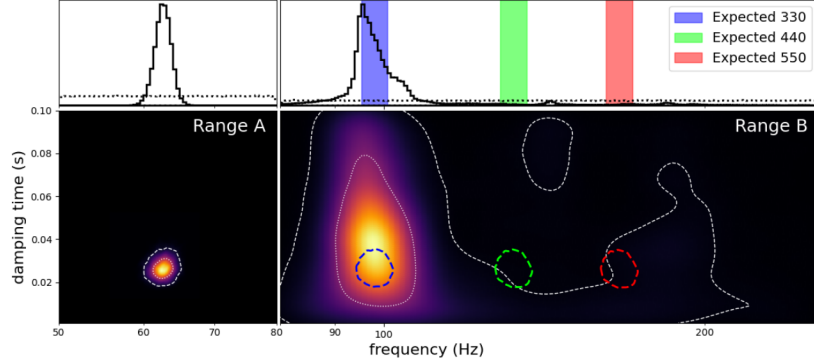
Figure 1.2: Posterior distribution of frequency and damping time for the event GW190521[3]. There are two modes visible for this event. The $l = m = 2$ mode which corresponds to the bright region in Range A and $l = m = 3$ mode which is the bright region in Range B. These are the same frequency ($\omega_{lmn}/2\pi$) and damping time (τ_{lmn}) we have encountered in equation 1.5.

The analysis of GW data is performed under the GR formalism where the final object is described by the Kerr metric which characterizes the black hole with 2 parameters; Mass and Spin. As the reader will see in coming sections, we consider deviations from the known Schwarzschild and Kerr metrics by allowing additional parameters and we want to see the implications on the new parameters given the LIGO data. Namely, we adopt the Johanssen-Psaltis (JP) metric which is stationary and axisymmetric but not a vacuum solution of EFE. The motivation to use this as an alternate comes from its stationarity, axisymmetry and that it reduces to the Kerr case in the limiting case $\epsilon_3 \longrightarrow 0$. In principle, one can use any other metric that possesses these two properties. The additional parameters due to the JP metric are ϵ_k's and these affect the geometric structure of the spacetime and consequently the light ring properties. We have restricted ourselves to the case of a non-zero ϵ_3 because it is the first non-zero parameter after ϵ_0, ϵ_1 and ϵ_2. However, the same analysis can be performed for ϵ_k with $k > 3$ as well.

Having discussed the prerequisite knowledge, We will now dive in to the calculation of expressions for the observables, frequency and damping time, with the ultimate goal of measuring the likelihood of non-Kerr parameters. We get right into the calculations part of this thesis by calculating the physical properties of null orbits in different scenarios. A black hole and a test particle's 4-velocity is

5

the starting point for our calculations and then we consider the case of a photon. This text is written such that it is increasing in complexity. As the text progresses, the reader will notice the following trend:

Newtonian $\longrightarrow$ Schwarzschild $\longrightarrow$ modified Schwarzschild $\longrightarrow$ Kerr $\longrightarrow$ modified Kerr $\longrightarrow$ post-Kerr $\longrightarrow$ ringdown analysis $\longrightarrow$ PyCBC.

1.3 Outline

Given the background discussed in section 1,1 and 1.2, we will go through the following milestones:

- Chapter 2 will calculate the light properties in known geometries, in their modifications and briefly discuss the calculation of quasi-normal modes (QNM)

- Chapter 3 will establish the validity of the QNM spectrum and discuss the Johanssen-Psaltis metric

- Chapter 4 will produce results for the two gravitational wave events: GW150914 and GW190521, and introduces the Bayesian inference package PyCBC and we run inference for GW150941

- Chapter 5 summarizes with a discussion and possible future directions

- Chapter 6 concludes the thesis

Chapter 2

Gravitational Null Orbits

One way of looking at black hole ringdowns is to calculate the properties of circular orbits in different scenarios because it turns out to give a good approximation to the frequency and damping times of gravitational wave the same. We are interested in the null circular orbits in different situations where a photon/graviton is orbiting a source mass. It turns out and the reader will see that period of a circular orbit calculated in Newtonian mechanics happens to match exactly with the period of a particle orbiting a Schwarzschild black hole. We will also see the coincidence that the location of the peak of the potential affecting a test scalar field in the Schwarzschild case is the same as the location we find using Keplar's third law. With these ideas in mind. Let us now have a look at the steps required to reach the above stated prophecies.

2.1   Newtonian case

In Newtonian mechanics, Kepler's third law gives the relation between the radius and period of the circular orbit of a particle gravitationally bound to a source

mass:

$$F_{centripetal} = F_{gravity}$$

$$\frac{mv^2}{r} = \frac{Mm}{r^2}$$

$$\frac{m\omega^2 r^2}{r} = \frac{Mm}{r^2}$$

$$T^2 = \frac{4\pi^2}{M}r^3 \tag{2.1}$$

Since Newtonian gravity is the limiting case of GR, the same relation must be recovered when the gravitational field is weak. The geodesic equation gives the equation of motion of the particle in the 4-vector formalism.

2.2   Schwarzschild Black Holes

We go one step forward in complexity and now consider the Schwarzschild metric:

$$dS^2 = -\Delta(r)dt^2 + \frac{dr^2}{\Delta(r)} + r^2 d\Omega^2 \tag{2.2}$$

$$g_{\mu\nu} = \begin{bmatrix} -\Delta(r) & 0 & 0 & 0 \\ 0 & \frac{1}{\Delta(r)} & 0 & 0 \\ 0 & 0 & r^2 & 0 \\ 0 & 0 & 0 & r^2\sin^2\theta \end{bmatrix} \tag{2.3}$$

where, $\Delta(r) = (1 - \frac{r_s}{r}), \ \ r_s = 2M$

We choose the 4-Velocity of the particle to be:

$$U^\alpha = \begin{pmatrix} A, & 0, & 0, & B \end{pmatrix}$$

so that the there is no dependence on the r and θ components, making the calculation easier. If we set A and B to 0 as well, the particle would stay at a point in spacetime. We make this choice because we only consider the $\theta = \pi/2$ plane and a particular $r = r_{ph}$. This means that the position of the particle does not change in the r and θ directions. Plus, the goal of this section is to find the value of r_{ph}.

A timelike geodesic has the property

$$U^\alpha U_\alpha = -1 \tag{2.4}$$

$$-\Delta A^2 + r^2 \sin^2\theta B^2 = -1 \tag{2.5}$$

We do not need this property here but it is important to be mentioned for the light-like case. The geodesic equation allows us to handle 4-vectors to find the orbital period for any circular orbit.

$$U^\alpha \nabla_\alpha U^\beta = 0 \tag{2.6}$$

Where ∇_α is the covariant derivative given by:

$$\nabla_\alpha U^\beta = \partial_\alpha U^\beta + \Gamma^\beta_{\ \alpha\kappa} U^\kappa \tag{2.7}$$

The components of the chosen 4-velocity are functions of t and ϕ, the term $\partial_\alpha U^\beta$ is zero and we only need to compute the Christoffel symbols $\Gamma^\beta_{\ \alpha\kappa}$ in the Schwarzschild geometry. The only relevant non-zero Christoffel symbols for this case are:

$$\Gamma^r_{\ tt} = \frac{1}{2}\left(\frac{r_s}{r^2} + \frac{r_s^2}{r^3}\right), \ \Gamma^r_{\ \phi\phi} = r_s - r \tag{2.8}$$

These are the only relevant ones because of the choice of our 4-velocity. These correspond to the radial geodesic equation and using them in (2.6) we have,

$$\frac{M}{r^3} = \left(\frac{B}{A}\right)^2 \tag{2.9}$$

We also know that ϕ-component is the $\frac{d\phi}{d\tau}$ and the r-component is $\frac{dr}{d\tau}$ where τ is the affine parameter of motion. Hence, using chain rule:

$$\frac{d\phi}{dt} = \frac{\frac{d\phi}{d\tau}}{\frac{dt}{d\tau}}$$
$$\text{where, } \frac{d\phi}{dt} = \frac{B}{A} \tag{2.10}$$

We can now use integration to find the orbital period:

$$\int_0^{2\pi} d\phi = \int_o^T \frac{B}{A} dt$$

$$2\pi = \sqrt{\frac{M}{r^3}} T$$

$$T^2 = \frac{4\pi^2}{M} r^3 \tag{2.11}$$

We have successfully found the period of a particle on a circular orbit around the source mass in the Schwarzschild case and it is indeed the same as the Newtonian period.

Now we specify that the particle is light-like and impose the Null condition. A light-like particle is one that travels at the speed of light, such as a photon/graviton and obeys the property:

$$U^\alpha U_\alpha = 0 \tag{2.12}$$

$$-\Delta A^2 + r^2 \sin^2\theta B^2 = 0 \tag{2.13}$$

We can use the same chain rule followed by integration to find the orbital period of a light-like particle:

$$\frac{B}{A} = \sqrt{\frac{\Delta}{r^2}}$$

$$\int_0^{2\pi} d\phi = \int_o^{T'} \frac{B}{A} dt$$

$$2\pi = \sqrt{\frac{\Delta}{r^2}} T'$$

$$T'^2 = \frac{4\pi^2}{\Delta} r^2 \tag{2.14}$$

This is the orbital period of a photon travelling in a circular orbit around the black hole. We already know the orbital period of any circular orbit regardless of the properties of the test particle. It is not surprising that equation 2.14 is different from equation 2.11. This is because the geodesic equation does not take the nature of the particle into consideration. 2.14 is an additional condition which is only valid for light-like particles. The photon's orbital period T' must coincide with

the T we calculated from the geodesic equation for any circular orbit. Therefore,

$$T'^2 = T^2$$
$$\frac{4\pi^2}{\Delta}r^2 = \frac{4\pi^2}{M}r^3$$
$$r = \frac{M}{\Delta}$$
$$r = \frac{M}{\left(1 - \frac{r_s}{r}\right)}$$
$$r = 3M \tag{2.15}$$

The radial position $r = 3M$, which we had called r_{ph} earlier, is the location of a light ring in the Schwarzschild spacetime. Any light-like particle (photons, gravitons) will have circular orbits at $r_{ph} = 3M$ Using equation 2.15 in the orbital period equation 2.14:

$$T'^2 = \frac{4\pi^2}{\Delta}r^2$$
$$T'^2 = \frac{4\pi^2}{\left(1 - \frac{r_s}{r}\right)}r^2$$
$$T'^2 = \frac{4\pi^2}{\left(1 - \frac{r_s}{3M}\right)}(3M)^2$$
$$\omega = \frac{1}{3\sqrt{3}M} \tag{2.16}$$

We have now reached the goal of our calculation and found the orbital frequency of a photons/gravitons orbiting a Schwarzschild black hole.

This result does not account for a perturbed Schwarzschild black hole, the black holes we are dealing with are ringing down i.e perturbed and must have have a decaying orbital frequency as the photon leaves the light ring location. This is referred to as a quasi-normal mode (QNM) and we need to be more specific in our calculation by introducing some perturbation to the Schwarzschild black hole and make use of spherical harmonics. The next section helps us find the QNM spectrum of a perturbed Schwarzschild black hole.

2.3 Spherical Harmonics (l,m,n)

This formalism [4] reduces the equation of a test scalar field to a wave equation which has eikonal quasi-normal mode (QNM) solutions. The eikonal approximation is widely used in wave scattering computations, allowing the calculation to be simplified by assuming that the wave scatters in a a special direction and reduces the system to a differential equation of one variable. For the situation at hand, the scattering takes place due to the perturbation in the spacetime. This section will provide an overview of the calculation in Schwarzschild background. What we are trying to do is solve EFE for a metric that is close to Schwarzschild is different due to the presence of a scalar field. This is similar to the standard calculation of finding gravitational waves by introducing a perturbation to an exact and know solution of EFE such as the Schwarzschild metric. A massless scalar test field ϕ in the background Schwarzschild metric ($g_{\mu\nu}^B$) obeys the Klein-Gordon equation:

$$\Box\phi = \frac{1}{\sqrt{-g^B}}\partial_\mu(\sqrt{-g^B}g_B^{\mu\nu}\partial_\nu)\phi = 0 \tag{2.17}$$

where $\Box$ is the D'Alembert operator and g^B is the determinant of the Schwarzschild metric.

Since the background is spherically symmetric, ϕ can be written in terms of spherical harmonics which are represented by Legendre polynomials $Y_{lm}(\theta, \phi)$.

$$\phi(t, r, \theta, \phi) = \frac{1}{r}\sum_{l=0}^{\infty}\sum_{m=-l}^{l}\phi_{lm}(t, r)Y_{lm}(\theta, \phi) \tag{2.18}$$

substituting $\phi(t, r, \theta, \phi)$ in 2.17, the following expression in obtained:

$$\Delta\partial_r(\Delta\partial_r\phi_{lm}) - \partial_t^2\phi_{lm} - V_l^\phi(r)\phi_{lm} = 0 \tag{2.19}$$

where $V_l^\phi(r) = \Delta(\frac{l(l+1)}{r^2} + \frac{2M}{r^3})$. This is a radial potential that affects the orbital properties.

Moving to a tortoise coordinate ($r \longrightarrow x$), a coordinate transformation such that $x \longrightarrow \infty$ as the observer approaches the event horizon

$$x \equiv r + 2M\ln\frac{r - 2M}{2M} \tag{2.20}$$

and Fourier transforming ϕ modifies the wave equation and makes the calculation easier. Then, the relevant expression for QNM calculation becomes:

$$\partial_x^2 \tilde{\phi}_{lm} + [\omega^2 - V_l^\phi]\tilde{\phi}_{lm} = 0 \qquad (2.21)$$

Recall that one can have the three types of perturbations to the metric; scalar, vector and tensorial. Equation 2.21 holds for scalar perturbation (spin = 0) as well as tensor perturbations (spin = 2) with even (+, polar) and odd (-, axial) parity such that:

$$\partial_x^2 \psi_\pm + [\omega^2 - V_l^\pm(r)]\psi_\pm = 0 \qquad (2.22)$$

Notice that we have changed the function from ϕ to ψ to make the distinction clear. There are two kinds of potentials in the above equation, $V_l^-(r)$ is the Regge-Wheeler potential[5] and $V_l^+(r)$ is the Zerilli[6] potential. These are different because of the two kinds of tensorial perturbations, axial and polar respectively. The peaks of the potential, where $V'(r) = 0$, give the location of the light ring $(r = 3M)$.

Assuming the solution $\psi_\pm = A_\pm(x)\exp[\frac{\iota S_\pm(x)}{\epsilon}]$ where $S_\pm(x)$ is a phase function, and taking the double expansion $\epsilon << 1$ and $l >> 1$, equation 2.22 reduces to

$$-\frac{1}{\epsilon^2}(\partial_x S_\pm)^2 + \omega^2 - l^2 U = 0 \text{ with } U(r) = \frac{\Delta(r)}{r^2} \qquad (2.23)$$

$\partial_x S_\pm \longrightarrow 0$ at the the radial location $r = r_{ph}$ and the frequency calculated in an arithmetic fashion in section 2.2 is recovered from the above formalism with the addition of a factor of l which comes from the spherical harmonics.

$$\omega_R^{(0)} = l\sqrt{U(r_{ph})} = \frac{l}{3\sqrt{3}M} \qquad (2.24)$$

We still don't have the damping time for the QNM. In order to do that, we allow the $\omega's$ to be complex ($\omega = \omega_R + \iota\omega_I$) and adopt the ansatz

$$\omega_R = \omega_R^{(0)} + \omega_R^{(1)} + \mathcal{O}(l^{-1}), \quad \omega_I = \omega_I^{(1)} + \mathcal{O}(l^{-1}) \qquad (2.25)$$

Plugging this ansatz in the the tensorial wave equation and doing the same ex-

13

pansions again we find:

$$\frac{2\iota}{\epsilon}(\partial_x S_\pm)(\partial_x A_\pm) + (\frac{\iota}{\epsilon}\partial_x^2 S_\pm + 2\iota\omega_R^{(0)}\omega_I^{(1)} + 2\omega_R^{(0)}\omega_R^{(1)} - lU)A_\pm = 0 \qquad (2.26)$$

Now our expression now contains both, the real and imaginary parts of the frequency. This allows us to treat real and imaginary parts the expression independently. Again solving for the imaginary part in the bracket we find $\omega_I^{(1)}$, and the real part for $\omega_R^{(1)}$.

$$\omega_I^{(1)} = -\frac{1}{6\sqrt{3}M} \qquad (2.27)$$

$$\omega_R^{(1)} = \frac{1}{6\sqrt{3}M} \qquad (2.28)$$

Putting all of this back into our complex frequency:

$$\omega = (l + \frac{1}{2})\frac{1}{3\sqrt{3}M} - \iota\frac{1}{6\sqrt{3}M} \qquad (2.29)$$

Now we have the QNM frequency spectrum that depends on the spherical harmonics (l) and the damping time, which is independent of l.
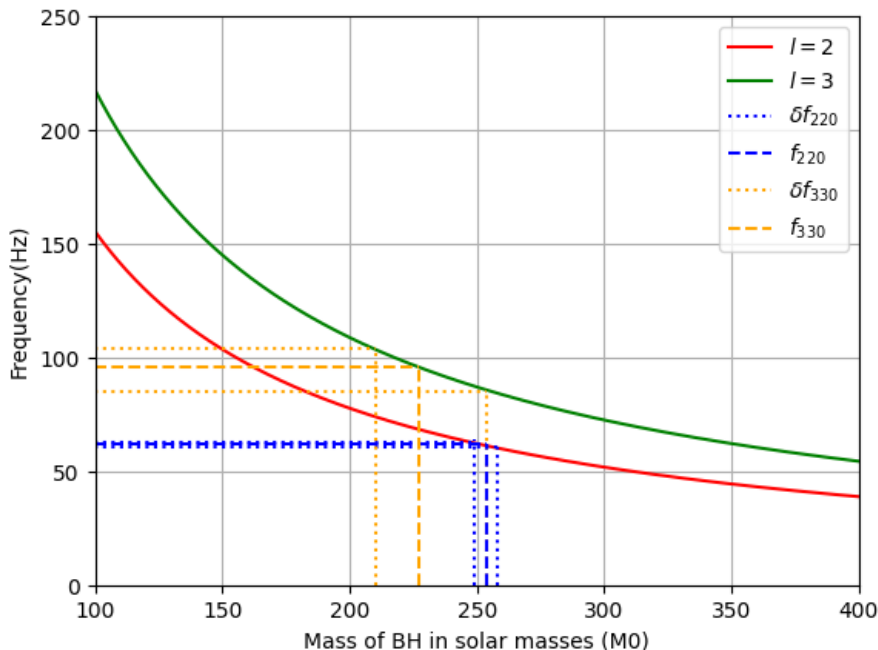
Figure 2.1: Frequency-Mass plot for $l = 2$ and $l = 3$ mode in the Schwarzschild background. For GW190521, the blue and yellow dashed lines represent the measured frequency values and and the dotted ones are the errors in the measurement. This is a naive test but still shows that Schwarzschild is not enough and we need to incorporate the spin of the black hole in the analysis.

2.4 Modified Schwarzschild (toy model)

It is interesting to see what happens if we keep the spherical symmetry and allow the Schwarzschild mass to be a function of r and not just a constant parameter. We introduce a new parameter "C" associated with the mass function such that $M(r) \rightarrow M - \frac{C}{2}r^{k-1}$. This is not the most general case as a modification can be achieved by any $M(r)$ with the condition that the geometry must be stationary and spherically symmetric. We make this choice because our objective is to simply observe what happens and the fact that it is generally easier to handle and

visualize polynomials. The geometry is still spherically symmetric with a new Δ_k;

$$\Delta_k(r) = 1 - \frac{2M(r)}{r} = 1 - \frac{2M}{r} + Cr^{k-2} \tag{2.30}$$

where M is the Schwarzschild mass and the C is the new parameter, of course depending on the index k. The metric then becomes:

$$g_{\mu\nu} = \begin{bmatrix} -\Delta_k(r) & 0 & 0 & 0 \\ 0 & \frac{1}{\Delta_k(r)} & 0 & 0 \\ 0 & 0 & r^2 & 0 \\ 0 & 0 & 0 & r^2\sin^2\theta \end{bmatrix}$$

The piece of information we need is the light ring position and frequency. We do not go into the calculation of the damping time unless something physically relevant is going on. Choosing a particular k changes the light ring position as expected and we also check if the resulting expression reduces to the Schwarzschild $r = 3M$ in the limit $C \longrightarrow 0$:

k-value	# of roots of $\omega_{null} - \omega_{geod} = 0$ (LR)	LR same as Schwarzschild case for C=0?
$\leq$ -1	piece-wise	yes
-1	3	yes
0	2 ($r = \frac{3M \pm \sqrt{-8C+9M^2}}{2}$)	yes
1	1 ($r = -1.5C + 3M$)	yes
2	1 ($r = \frac{3M}{C+1}$)	yes
3	2 ($r = \frac{-1 \pm 2.5\sqrt{CM+1/6}}{C}$)	yes
4	1 ($r = 3M$)	yes
$\geq$ 5	piece-wise	yes

TABLE I: The choice of k decides the LR position and consequently, the orbital frequency. This table shows some values of k and their corresponding LR positions Some of the k-values return piece-wise roots which means that the expression is valid for different values of C and M. We do not show the piece-wise

expressions as they are lengthy and uninteresting.

2.4.1 Schwarzschild - de Sitter Case

The interesting situation out of the ones tabulated in Table 1 is when $k = 4$, where we have the Schwarzschild - de Sitter case with $M(r) \rightarrow M - \frac{C}{2}r^3$. The new parameter C is then identified as the cosmological constant Λ in EFE.

$$\Delta_4(r) = 1 - \frac{2M(r)}{r} = 1 - \frac{2M}{r} + \Lambda r^2 \tag{2.31}$$

$\Delta_4(r)$ necessarily affects the metric components 2.3 and consequently the light ring properties. However, this metric also admits the same light ring position as the Schwarzschild case ($r = 3M$) and going forward with the eikonal QNM calculation we find:

- As shown in Table I, the light ring position does not change i.e. it is still $r = 3M$.

- The frequency and damping times, both, change by a factor of $\sqrt{1 + 27M^2\Lambda}$.

This means that we can use observational data and study it under the Schwarzschild - de Sitter background and try to infer the value of Λ. We use the frequency and damping time measurements of the event GW190521. Plotting the $\Lambda - M$ curves for the 220 and 330 mode frequencies and damping time, we have the following result:
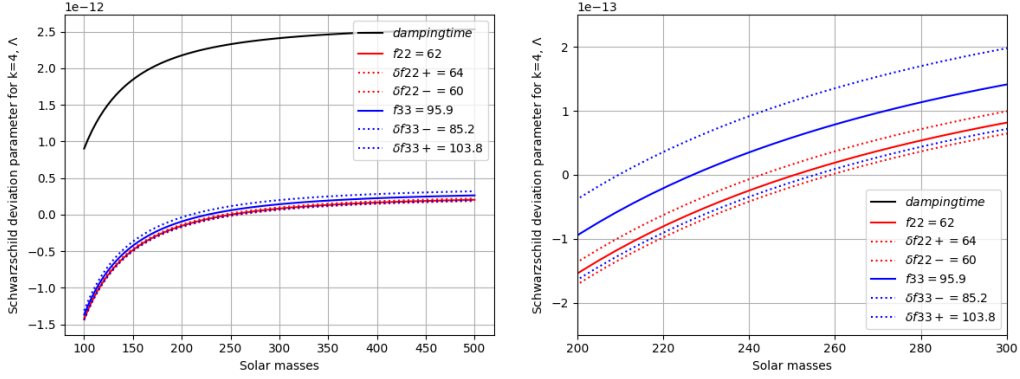
(a) The frequency and damping times in the Schwarzschild - de Sitter case, the parameter C is identified with the cosmological constant, Λ. With this calculation we see that Λ is of the order of 10^{-12} in SI units. This is about 40 orders of magnitude away from the current value of Λ and means that Schwarzschild - de Sitter is not a good candidate for measuring Λ.

(b) Zoomed in. For $\Lambda = 0$, the corresponding Mass values of the two modes are similar to Figure 2.1 up to truncation errors in Python.

Having looked at the Schwarzschild metric and analyzed its light ring structure, we are now ready to move on to a more complex system by considering spinning black holes described by the Kerr metric. From here on, we will consider spinning black holes only and add new parameters just as we did with non-spinning, Schwarzschild black holes.

2.5   Kerr Black Holes

The Kerr solution is a stationary, axisymmetric solution to Einstein's equation. It includes two parameters, mass(M) and spin(a) and reduces to the Schwarzschild

metric if $a \longrightarrow 0$. In Boyer-Lindquist coordinates, the Kerr metric reads:

$$ds^2 = -(1 - \frac{r_s r}{\Sigma})dt^2 + \frac{\Sigma}{\Delta}dr^2 + \Sigma d\theta^2$$
$$+ (r^2 + a^2 + \frac{r_s r a^2 \sin^2 \theta}{\Sigma}) \sin^2 \theta d\phi^2 - \frac{2 r_s r a \sin^2 \theta}{\Sigma} dt d\phi \qquad (2.32)$$

$$g_{\mu\nu} = \begin{bmatrix} -(1 - \frac{r_s r}{\Sigma}) & 0 & 0 & -\frac{r_s r a \sin^2 \theta}{\Sigma} \\ 0 & \frac{\Sigma}{\Delta} & 0 & 0 \\ 0 & 0 & \Sigma & 0 \\ -\frac{r_s r a \sin^2 \theta}{\Sigma} & 0 & 0 & (r^2 + a^2 + \frac{r_s r a^2 \sin^2 \theta}{\Sigma}) \sin^2 \theta \end{bmatrix} \qquad (2.33)$$

We perform the same calculations for the Kerr metric as in the Schwarzschild case. Keep in mind that any result found in this section will only correspond to photon orbits of an unperturbed black hole. To accommodate for a ringdown, we will have to introduce perturbations. This is taken care of in section 2.7.

Proceeding with the calculation using the Null condition and the Geodesic equation for the Kerr Metric:

$$U^\alpha U_\alpha = 0 \qquad (2.34)$$

$$-(1 - \frac{r_s r}{\Sigma})A^2 + (r^2 + a^2 + \frac{r_s r a^2 \sin^2 \theta}{\Sigma})B^2 - \frac{r_s r a \sin^2 \theta}{\Sigma}(2AB) = 0 \qquad (2.35)$$

$$\frac{B^2}{A^2}(r^2 + a^2 + \frac{r_s a^2}{r}) - \frac{B}{A}(2r_s a) - (r - r_s) = 0 \qquad (2.36)$$

Notice that now there are quadratic as well as linear terms in B/A because of the non-zero $g_{t\phi} = g_{\phi t}$ terms in the metric. Solving the quadratic equation for $\frac{B}{A}$:

$$\frac{B}{A} = \frac{2r_s a \pm \sqrt{-4r_s r^3 - 4r_s a^2 r + 4r^4 + 4a^2 r^2 + 4r r_s a^2}}{2r^3 + 2a^2 r + 2r_s a^2} \qquad (2.37)$$

This is the orbital frequency of a massless particle orbiting a Kerr black hole. Just to check if this result goes to the Schwarzschild case if $a \longrightarrow 0$,

$$\frac{B}{A} = \omega = \frac{\sqrt{4r_s r^3 + 4r^4}}{2r^3} = \frac{\sqrt{1 - \frac{r_s}{r}}}{r} \qquad (2.38)$$

which is the same as the orbital frequency of a massless particle in the Schwarzschild case, equation 2.14. Now we need the geodesic equation to find the orbital fre-

quency of any circular orbit around a Kerr black hole.

$$U^\alpha \nabla_\alpha U^\beta = 0 \tag{2.39}$$

Where ∇_α is the covariant derivative given by:

$$\nabla_\alpha U^\beta = \partial_\alpha U^\beta + \Gamma^\beta_{\ \alpha\kappa} U^\kappa \tag{2.40}$$

Again, the term $\partial_\alpha U^\beta$ is zero and we only need to handle the second half of equation 2.40. Furthermore,the only relevant non-zero Christoffel symbols for the Kerr case are:

$$\Gamma^r_{\ tt} \, , \ \Gamma^r_{\ t\phi} \, , \ \Gamma^r_{\ \phi t} \, , \ \Gamma^r_{\ \phi\phi} \, , \ \Gamma^\phi_{\ tt} \, , \ \Gamma^\phi_{\ t\phi} \, , \ \Gamma^\phi_{\ \phi t} \, , \ \Gamma^\phi_{\ \phi\phi} \tag{2.41}$$

All Christoffel symbols of the form $\Gamma^\theta_{\ \alpha\beta}$ terms are zero for the equatorial plane ($\theta = \frac{\pi}{2}$). Plugging these in the geodesic equation we have:

$$0 = \frac{B^2}{A^2}(r_s a^2 r - 2r^4) - \frac{B}{A}(2arr_s) + r_s r \tag{2.42}$$

$$\tag{2.43}$$

Solving the quadratic equation for $\frac{B}{A}$:

$$\frac{B}{A} = \frac{2arr_s \pm \sqrt{8r^5 r_s}}{2r_s r a^2 - 4r^4} \tag{2.44}$$

Once again to check for the limiting case $a \longrightarrow 0$

$$\frac{B}{A} = \omega = \frac{\sqrt{8r^5(r_s)}}{4r^4} = \frac{\sqrt{r^5 M}}{r^4} \tag{2.45}$$

$$\omega = \frac{2\pi}{T} = \frac{\sqrt{r^5 M}}{r^4} \tag{2.46}$$

$$\frac{4\pi^2}{T^2} = \frac{r^5 M}{r^8} = \frac{M}{r^3} \tag{2.47}$$

Which is same as the period calculated in the Schwarzschild case, equation 2.11. Following the same procedure as in the previous sections, the expression we get after equating the Null frequency and the Geodesic frequency can be solved to

find the position of the light ring in the Kerr geometry and is given by[7]:

$$r_{ph} = 2M(1 + \cos{[\frac{2}{3} \cos^{-1}{(\frac{a}{M})}]})$$

(2.48)

and the light ring frequency is given by[8]:

$$\omega = \frac{1}{M}(\frac{a}{M} + (\frac{r}{M})^{3/2})^{-1}$$

(2.49)

Notice that we have not yet calculated the damping time has not for the Kerr geometry. It is found by computing the Lyapunov exponent of the light ring orbits and is addressed in section 2.8 which calculates the general expressions for light ring position, frequency and damping time.

2.6   Modifying Kerr

We want to see what happens if, once again, we allow the mass parameter to be a function of r and check the implications on the frequency. This time we do not specify a particular form of the function as in Schwarzschild. Instead we Taylor expand a general mass function $M(r)$ and the coordinate r around the light ring location (r_{ph}) to first order in ϵ as follows:

$$M(r) \longrightarrow M_0 + M'(r)r\epsilon$$

(2.50)

We have already seen in the Schwarzschild case that allowing $M(r)$ changes the light ring position depending on the explicit form of the function. As such, we expect the light ring position to change and keep terms up to linear order in the expansion parameter ϵ:

$$r \longrightarrow r_{ph} + \delta_r\epsilon$$

(2.51)

This $M(r)$ will of course affect the components of the metric and we write the metric such that $\mathcal{O}(\epsilon)$ represent the term away from the Kerr component and linear

in ϵ.

$$g_{\mu\nu} = \begin{bmatrix} g_{tt}^0 + \mathcal{O}(\epsilon) & 0 & 0 & g_{t\phi}^0 + \mathcal{O}(\epsilon) \\ 0 & g_{rr}^0 + \mathcal{O}(\epsilon) & 0 & 0 \\ 0 & 0 & g_{\theta\theta}^0 + \mathcal{O}(\epsilon) & 0 \\ g_{\phi t}^0 + \mathcal{O}(\epsilon) & 0 & 0 & g_{\phi\phi}^0 + \mathcal{O}(\epsilon) \end{bmatrix}$$

Using this $M(r)$ in place of M in the Kerr metric, we equate the Null orbital frequency equation and Geodesic orbital frequency equation again to reveal the relation:

$$\begin{aligned} 0 = & \sqrt{\Delta}(r^3 - a^2(M(r) - M'(r)r)) \\ & + a(2M(r)r^2 + (r^2 + a^2)(M(r) - M'(r)r)) \\ & - rg_{\phi\phi}\sqrt{r(M(r) - M'(r)r)} \end{aligned} \tag{2.52}$$

In the case where $M'(r) = 0$, the roots of this equation is the r_{ph} shown in equation 2.48. Plugging the Taylor expansions into the above expression and only keeping the terms linear in ϵ, we find that the change in the light ring position is linearly dependent on the first derivative of the mass function up to a constant.

$$\delta_r = \frac{r_{ph}\sqrt{M_0 r_{ph}}(-2\sqrt{\Delta_0}a(a\sqrt{M_0 r_0} - r_{ph}{}^2) + a^2 M_0 - r_{ph}{}^3)}{D}M'(r) \tag{2.53}$$

where

$$\begin{aligned} D = & -\sqrt{\Delta_0}M_0(2a^2 M_0 + a^2 r_{ph} + r_{ph}{}^3) \\ & + \sqrt{\Delta_0 M_0 r_{ph}}(3\sqrt{\Delta_0}r_{ph}{}^2 - a^2\sqrt{M_0 r_{ph}} + 6aM_0 r_{ph} - 3r_{ph}{}^2\sqrt{M_0 r_{ph}}) \\ & + \sqrt{M_0 r_{ph}}(a^2 M_0{}^2 - 2a^2 M_0 r_{ph} - M_0 r_{ph}{}^3 + 2r_{ph}{}^4)) \end{aligned} \tag{2.54}$$

Plugging the same Taylor expansion and using the above result in the Null frequency, again only keeping the terms linear in ϵ, the change in the frequency is again found to be linearly dependent on the first derivative of the mass function up to a constant, $\mathcal{C}$, which is also in terms of r_{ph}, M_0 and the metric components of the Kerr geometry.

$$\delta_\omega = \mathcal{C}M'(r) \tag{2.55}$$

We are slowly building towards trying to understand a post-Kerr metric, which

we discuss in chapter 3.

2.7 Teukolsky Master Equation and Quasi-normal modes

In an axisymmetric geometry, we can no longer make use of the spherical harmonics as in Schwarzschild. We must now invoke spheroidal harmonics where the geometric object is a spheroid.
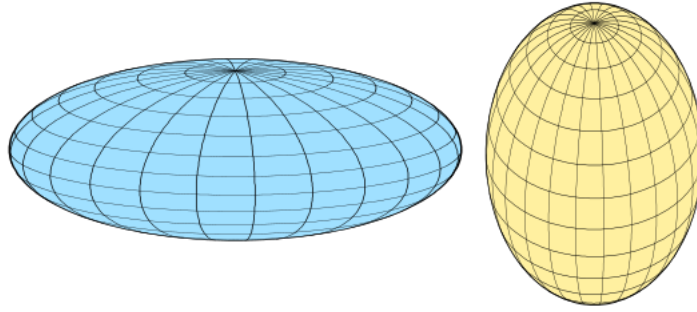

Figure 2.2: Spheroids with vertical rotational axes. The structure on the left corresponds to oblate spheroids and on the right corresponds to prolate ones.

The Kerr metric, as we already know, is axisymmetric and its ergosphere, the region outside the horizon of a rotating black hole, can be visualized with the above picture. The calculation of QNMs under this geometry is also modified by changing the ansatz of the wave function from spherical to spheroidal. This increases the complexity of the calculation and we need to adopt the Teukolsky Master Equation for the Kerr metric. We will briefly outline the procedure in this section and conclude with Teukolsky's findings.

Saul Teukolsky calculated the QNMs in a Kerr background by using the the Newman-Penrose formalism[9] to find decoupled partial differential equations perturbatively. The null tetrad consists of the following 4 null vectors, l^μ, n^μ, m^μ and $m^{*\mu}$. l and n are real, m is complex and m^* is its conjugate. The null vectors must satisfy have normalization $l^\mu n_\mu = 1$ and $m^\mu m_\mu^* = -1$. The next piece we want is the Weyl Tensor, $C_{\alpha\beta\gamma\delta}$, which is the trace free Riemann Tensor. Combining these two pieces under the NP formalism, we arrive at the 5 Newman-

Penrose complex scalars defined as follows:

$$\psi_0 = -C_{\alpha\beta\gamma\delta} \, n^\alpha m^\beta n^\gamma m^\delta \tag{2.56}$$

$$\psi_1 = -C_{\alpha\beta\gamma\delta} \, n^\alpha l^\beta n^\gamma m^\delta \tag{2.57}$$

$$\psi_2 = -C_{\alpha\beta\gamma\delta} \, m^{*\alpha} l^\beta n^\gamma m^\delta \tag{2.58}$$

$$\psi_3 = -C_{\alpha\beta\gamma\delta} \, m^{*\alpha} l^\beta n^\gamma l^\delta \tag{2.59}$$

$$\psi_4 = -C_{\alpha\beta\gamma\delta} \, m^{*\alpha} l^\beta m^{*\gamma} l^\delta \tag{2.60}$$

The choice of the null vectors depends on the spacetime we want to describe. Perturbatively, the tetrad can be written as a sum of the background and the perturbation:

$$l^\mu = l^{\mu A} + l^{\mu B} \tag{2.61}$$

$$n^\mu = n^{\mu A} + n^{\mu B} \tag{2.62}$$

$$m^\mu = m^{\mu A} + m^{\mu B} \tag{2.63}$$

$$m^{*\mu} = m^{*\mu A} + m^{*\mu B} \tag{2.64}$$

$$\tag{2.65}$$

where the A and B correspond to the the background and the perturbation, respectively. Plugging these into the NP formalism and only keeping terms up to first order in B, the relevant NP complex scalars are ψ_0^B and ψ_4^B for any Petrov type D metric.

A metric expressed in terms of the null tetrad is

$$g^{\mu\nu} = l^\mu n^\nu + n^\mu l^\nu - m^\mu m^{*\nu} - m^{*\mu} m^\nu \tag{2.66}$$

and substituting the Kerr versions of the null tetrad, brings us to the famous Teukolsky master equation:

$$\left[\frac{(r^2 + a^2)^2}{\Delta} - a^2 \sin^2\theta \right] \frac{\partial^2 \psi}{\partial t^2} + \frac{4Mar}{\Delta} \frac{\partial^2 \psi}{\partial t \partial\varphi} + \left[\frac{a^2}{\Delta} - \frac{1}{\sin^2\theta} \right] \frac{\partial^2 \psi}{\partial\varphi^2}$$
$$- \Delta^{-s} \frac{\partial}{\partial r} \left(\Delta^{s+1} \frac{\partial\psi}{\partial r} \right) - \frac{1}{\sin\theta} \frac{\partial}{\partial\theta} \left(\sin\theta \frac{\partial\psi}{\partial\theta} \right) - 2s \left[\frac{a(r-M)}{\Delta} + \frac{\iota\cos\theta}{\sin\theta} \right] \frac{\partial\psi}{\partial\varphi}$$
$$- 2s \left[\frac{M(r^2 - a^2)}{\Delta} - r - \iota a\cos\theta \right] \frac{\partial\psi}{\partial t} + (s^2 \cot^2\theta - s)\psi = 4\pi\Sigma T \tag{2.67}$$

The s corresponds to the type of perturbation introduced and is called the spin weight of the field. $s = 0$ corresponds to scalar fields, $s = \pm1/2$ corresponds to fermionic fields, $s = \pm1$ corresponds to electromagnetic fields and finally $s = \pm2$ corresponds to gravitational fields. Since we are interested in the gravitational perturbations to the Kerr metric, we will stick to the $s = \pm2$ case and also restrict ourselves to the vacuum case where $T = 0$. In this scenario, we use the separation of variables technique and assume a solution of the form

$$\psi = e^{-\iota \omega t} F(r, \theta, \phi) \tag{2.68}$$

$$\text{with, } F(r, \theta, \phi) = \sum_{l,m} e^{\iota m \phi} S_l^m(\theta) R_{\omega l m}(r) \tag{2.69}$$

This allows us to write the huge expression 2.67 into smaller chunks for the functions $S_l^m(\theta)$ and $R_{\omega l m}(r)$. We do not go about trying to solve these equations in this text, but highlight the key outcomes of Teukolsky's work. For the angular part, the relevant differential equation is:

$$\frac{1}{\sin \theta} \frac{d}{d\theta} \left(\sin \theta \frac{dS}{d\theta} \right) + \left(a^2 \omega^2 \cos^2 \theta - \frac{m^2}{\sin^2 \theta} - 2a\omega s \cos \theta \right.$$
$$\left. - \frac{2ms \cos \theta}{\sin^2 \theta} - s^2 \cot^2 \theta + E - s^2 \right) S = 0 \tag{2.70}$$

and for the radial equation:

$$\Delta \frac{d^2 R}{dr^2} + 2(s+1)(r - M) \frac{dR}{dr} + \left(\frac{K^2 - 2\iota s(r - M)K}{\Delta} = 4\iota \omega s r - \lambda \right) R = 0 \tag{2.71}$$

where E are the eigenvalues of the differential equation, $K \equiv (r^2 + a^2)\omega - am$ and $\lambda \equiv E - 2am\omega + a^2\omega^2 - s(s+1)$. Further manipulation of the angular equation is required which essentially provides the spin weighted spherical harmonics in terms of Legendre polynomials as such

$$S(\theta) = Y_l^m(\theta), \;\; l = |s|, |s| + 1 \ldots \tag{2.72}$$

$$E = l(l+1), \;\; -l \leq m \leq +l \tag{2.73}$$

The radial equation finds regular and irregular radial solutions when the $s = \pm2$ case is considered. These solutions can be thought of as incoming and outgoing at the horizon and the WKB method helps with solving the problem at hand. This

is denoted by considering the fraction Z_{out}/Z_{in} in the limiting case of $\omega \longrightarrow 0$

$$\frac{Z_{out}}{Z_{in}} = \frac{16\omega^4}{(l-1)(l+1)(l+2)}[1 + \mathcal{O}(a\omega)], \quad a\omega \ll 1 \tag{2.74}$$

Conveniently defining

$$Z(a,\omega,l,m) \equiv \left| \frac{Z_{out}}{Z_{in}} \frac{(l-1)(l+1)(l+2)}{16\omega^4} \right| \tag{2.75}$$

which has the symmetry property under complex conjugation of the radial equation

$$Z(a,\omega,l,m) = Z(a,-\omega,l,-m) \tag{2.76}$$

. Figures 2.3 (a) and (b) are taken from Teukolsky's paper and demonstrate his results for $l = m = 2$ and $l = m = 3$, the two modes we are interested in.

(a)   (b)
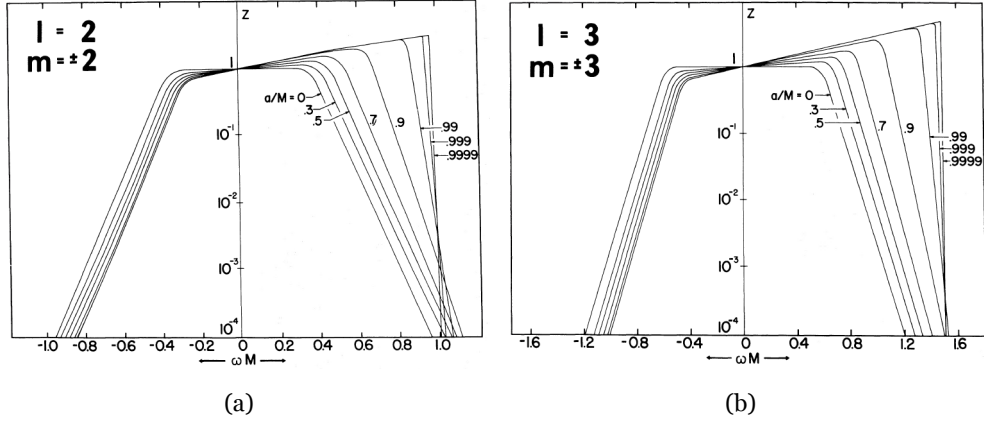
Figure 2.3: These figures show numerical results from Teukolsky's paper[10] for the two modes, $l = m = 2$ and $l = m = 3$. The quantity on the horizontal axis is the dimensional frequency and the vertical axis is the quantity Z defined earlier. In the limit case $\omega \longrightarrow 0$, we that the plot converges to $Z = 1$. Another noteworthy observation is that higher modes correspond to higher frequencies.

Expressed in a similar way as we wrote the Schwarzschild QNM spectrum, the

eikonal-limit Kerr QNM spectrum is:

$$\omega_R = l\Omega, \quad \omega_I = -(n + \frac{1}{2})\frac{|\gamma|}{2} \tag{2.77}$$

where Ω and γ are the orbital frequency and the damping time, respectively. It should be noted that there are multiple technicalities involved in this computation which are purposely being omitted since this calculation is not the main goal of this text. The reader is directed toward the original series of papers[11, 10], which is much more detailed.

2.8 Light ring in a general stationary axisymmetric spacetime

The goal now is to compute general expressions for a stationary axisymmetric spacetime which we will then apply to a particular metric in section 4.4. Let us assume that there exists a metric:

$$g_{\mu\nu} = \begin{bmatrix} -g_{tt} & 0 & 0 & g_{t\phi} \\ 0 & g_{rr} & 0 & 0 \\ 0 & 0 & g_{\theta\theta} & 0 \\ g_{\phi t} & 0 & 0 & g_{\phi\phi} \end{bmatrix}$$

that describes a stationary axisymmetric spacetime and allow the 4-velocity of the test particle to have radial component C as well. Since the interest is only in equatorial orbits only, θ-component of the 4-velocity is zero:

$$U^\alpha = \begin{pmatrix} A, & C, & 0, & B \end{pmatrix}$$

Physically, the t-component of the 4-velocity represents the conserved energy, $-A = E$ of the orbit and the ϕ-component represents the conserved angular momentum, $B = L$. Now to write down the equivalent of equation 63; the equation of motion in curved spacetime:

$$A^2 g_{tt} + 2AB g_{t\phi} + C^2 g_{rr} + B^2 g_{\phi\phi} = 0 \tag{2.78}$$

Notice that there are no terms in the θ-coordinate because the θ-component of the 4-velocity is zero. In order to make our lives easier and after a little algebra, the A and B can be written in terms of the metric components

$$A = \frac{g_{\phi\phi}E + g_{t\pi}L}{g_{t\phi}^2 - g_{tt}g_{\phi\phi}} \tag{2.79}$$

$$B = -\frac{g_{tt}L + g_{t\pi}E}{g_{t\phi}^2 - g_{tt}g_{\phi\phi}} \tag{2.80}$$

Additionally, as we now know that the ratio of B to A corresponds to $\frac{d\phi}{dt}$, the orbital frequency is given by:

$$\frac{B}{A} = \frac{d\phi}{dt} = -\frac{g_{tt}L + g_{t\pi}E}{g_{\phi\phi}E + g_{t\pi}L} = \Omega \tag{2.81}$$

Combining these expressions and plugging back in equation 2.78:

$$g_{\phi\phi}E^2 + 2g_{t\phi}EL + g_{tt}L^2 = (g_{t\phi}^2 - g_{tt}g_{\phi\phi})g_{rr}C^2 \equiv V_{eff} \tag{2.82}$$

The V_{eff} here is due to the non-zero r-component of the 4-velocity and determines the radial behaviour of the particle in this spacetime. Setting the r-component to zero (meaning that the particle is turning at some radial location $r = r_{orb}$), returns the expression we have already found for closed orbits with the geodesic equation in the previous section. The above expression holds for any closed orbit and one can find the orbital frequency at the radius $r = r_{orb}$. There is another quantity that needs to be defined because we will use it in the following sections, the impact parameter. It is simply the ratio of the angular momentum to the energy of the orbit

$$b_{orb} = \frac{L}{E} = \frac{1}{\Omega_{orb}} \tag{2.83}$$

Since our concern is photon orbits at the radial location $r = r_{ph}$, where the peak of the potential lies and hence the condition to be met is:

$$V'_{eff}(r_{orb}) = 0 \tag{2.84}$$

The solution of the above equation is the position of the light ring which is denoted

by $r_{orb} = r_{ph}$. We denote all photon orbit related quantities with the subscript'ph', so that $b_{orb} = b_{ph}$ and $\Omega_{orb} = \Omega_{ph}$ at the location $r_{orb} = r_{ph}$. Rewriting equation 2.82 and its radial derivative in terms of b_{ph} take these forms:

$$g_{tt}(r_{ph})b_{ph}^2 + 2g_{t\phi}(r_{ph})b_{ph} + g_{\phi\phi}(r_{ph}) = 0 \tag{2.85}$$

$$g'_{tt}(r_{ph})b_{ph}^2 + 2g'_{t\phi}(r_{ph})b_{ph} + g'_{\phi\phi}(r_{ph}) = 0 \tag{2.86}$$

Solving these equations for the impact parameter b for the photon orbit at $r = r_{ph}$ gives

$$b_{ph} = \frac{-g'_{t\phi} \pm \sqrt{g'^2_{t\phi} - g'_{tt}g'_{\phi\phi}}}{g'_{tt}} \tag{2.87}$$

and using equation 2.83 we find the expression for the orbital frequency of the photon orbit:

$$\Omega_{ph} = b_{ph}^{-1} = \frac{g'_{tt}}{-g'_{t\phi} \pm \sqrt{g'^2_{t\phi} - g'_{tt}g'_{\phi\phi}}} \tag{2.88}$$

We have now found the orbital frequency of photon ring in a general axisymmetric spacetime. For the Kerr case, the expression is evaluated using the Kerr metric components and their derivatives to reach the well-known Kerr orbital frequency, equation 2.49.

We turn our attention to the Lyapunov exponent that gives the characteristic time during which the photons escape the light ring due to the perturbed geometry. The way to think about this is to consider photons approaching the light ring from infinity and grazing the light ring as if on a parabolic path with their turning point coinciding with the light ring. This means that the photon will tangentially touch the light ring and escape without being captured in the light ring. To do this mathematically, consider the Binet equation and assume an exponential solution where the argument of the exponent gives the characteristic timescale of this grazing. Formally we set out to solve the following equation

$$\frac{dU}{d\phi} = -U^2\frac{C}{B} \tag{2.89}$$

where C and B are the r- and ϕ-components of the 4-velocity of the photon. Ad-

ditionally, we have defined a new variable; $U = \frac{1}{r}$ so that we can have a Binet-like equation

$$\left(\frac{dU}{d\phi}\right)^2 = \frac{U^4(g_{t\phi}^2 - g_{tt}g_{\phi\phi})}{g_{rr}} \frac{g_{tt}b^2 + 2g_{t\phi}b + g_{\phi\phi}}{(g_{tt}b + g_{t\phi})^2} \equiv f(U) \qquad (2.90)$$

At the turning point, $U_{ph} = \frac{1}{r_{ph}}$ where r_{ph} is the location of the light ring and in this scenario also the periapsis of the parabolic trajectory of the incoming photon, the function $f(U_{ph})$ and it's derivative $f'(U_{ph})$ must vanish such that we have

$$f(U_{ph}) = f'(U_{ph}) = 0 = \frac{df}{dU}(U_{ph}) \qquad (2.91)$$

Close to the periapsis we can expand U so that and only keep the leading order term,

$$U = U_{ph} + \epsilon U_1 + \mathcal{O}(\epsilon^2) \qquad (2.92)$$

To incorporate the connection of the periapsis to the light ring, the leading order term needs to be such that it corresponds with the ϕ-component of the 4-velocity[12].

$$\frac{dU_1}{d\phi} = \pm\kappa_{ph}U_1 \qquad (2.93)$$

$$\text{where, } \kappa_{ph}^2 = \frac{1}{2}\frac{d^2 f}{dU^2}(U_{ph}) = \frac{f''(U_{ph})}{2U_{ph}^2}$$

This differential equation admits exponential solutions of the form $U_1 = Ce^{\pm\kappa_0\phi}$. Also know the orbital frequency of the light ring we can substitute $\phi = \Omega_{ph}t + const$ to rewrite the solution U up to leading order in ϵ, which is now a function of time:

$$U(t) = U_{ph} + \epsilon Ce^{\kappa_{ph}\Omega_{ph}t} \qquad (2.94)$$

and rescale C so that

$$U(t) = U_{ph} + \epsilon e^{\pm\gamma_{ph}t} \qquad (2.95)$$

$$\text{where, } \gamma_{ph} = |\kappa_{ph}\Omega_{ph}| \qquad (2.96)$$

We have now found the characteristic timescale, $\frac{1}{\gamma_{ph}}$, for incoming photons graz-

ing the light ring of a general stationary axisymmetric spacetime.

Chapter 3

Post-Kerr Approximation

In light of the previous section 2.8, it is essentially possible to build such an alternate metric that can be used to describe stationary and axisymetric spacetimes. Imposing the null condition and the geodesic equation one can find physically significant orbits such as the light ring in our case. Since these metrics are not particularly vacuum GR solutions, they allow for additional parameters like the $M'(r)$ in the section 2.6. With the condition that the metric must reduce to the Kerr metric in the limiting case, the additional parameters are deviations from the Kerr geometry. These deviations must be centered around 0 if GR is to be true and can be measured using the data from experiments like LIGO. The following sub-sections, establish the validity of the post-Kerr approximation, describe the overall recipe for finding deviations from the Kerr light ring due to a non-Kerr spacetime and then choose a particular case to analyze.

3.1 Validity for post-Kerr QNM.

Glampedakis et al.[12] describe the post-Kerr scenario and outline the track for finding the QNM spectrum up to numerical error in the new geometry. Given that we have eikonal limit formulae[13](σ^K) and the exact Kerr QNM frequency (ω^K) we can write down the following relation, with the superscript K denoting Kerr values:

$$\omega^K = \sigma^K + \beta^K \tag{3.1}$$

where β^K accounts for the offset between the exact and the eikonal limit frequencies. We introduce this new factor in order to facilitate our computation in the sense that we want to maintain this offset if we are to come up with a modified version of the Kerr QNM frequency. In the post-Kerr scenario, the eikonal limit QNM can be found by computing the light ring properties and is necessarily different from the Kerr scenario, we denote this with σ and use the observed QNM frequency ω^{obs} along with β^K so that we can write

$$\omega^{obs} = \sigma + \beta^K. \tag{3.2}$$

If ω^{obs} is exactly a Kerr signal then obviously $\sigma = \sigma^K$ and we are done. We are interested in a signal that is not Kerr and therefore we need to find this new template that describes the non-Kerr QNM frequency. The β^K offset function ensures that we are within reasonable bounds of describing the observation with a non-Kerr template σ. Furthermore, since we know that we are going beyond Kerr, it is reasonable to define

$$\sigma = \sigma^K + \delta\sigma \tag{3.3}$$

where $\delta\sigma$ is the deviation from the Kerr QNM frequency. The goal is to find this deviation, given some non-Kerr spacetime. Some details about β^K are provided in appendix A.2.

3.2   Recipe for light ring in the post-Kerr scenario

We turn our attention to computing the QNM frequency in a post-Kerr scenario. As addressed in previous sections, we need a total of four quantities to obtain the properties of the light ring, with the subscripts K and 0 representing the Kerr and non-Kerr quantities respectively:

- The metric expressed in perturbative form so that

$$g_{\mu\nu} = g_{\mu\nu}^K(r) + \epsilon h_{\mu\nu}(r) + \mathcal{O}(\epsilon^2).$$

  where we are only interested in terms up to linear order in ϵ.

- The light ring position

$$r_0 = r_K + \epsilon \delta r + \mathcal{O}(\epsilon^2)$$

- The light ring frequency

$$\Omega_0(r) = \Omega_K(r) + \epsilon \delta\Omega(r) + \mathcal{O}(\epsilon^2)$$

- The Lyapunov exponent of the orbit

$$\gamma_0(r) = \gamma_K(r) + \epsilon \delta\gamma(r) + \mathcal{O}(\epsilon^2)$$

Using the perturbative form of the metric helps simplify the computation because we already know the Kerr quantities. Glampedakis et al.[12] find the deviation terms in all of the above expressions in terms of the derivatives of $h_{\mu\nu}$ and the Kerr parameters M and a. These are summarized as follows:

$$
\begin{aligned}
\delta\Omega(r) = {}&\mp\frac{1}{4}\Omega^K\left(\frac{r}{M}\right)^{1/2}[2h'_{t\phi} + \Omega_K h'_{\phi\phi} \\
&+ \frac{\Omega_K}{M}(r^3 \pm 2aM^{1/2}r^{3/2} + Ma^2)h'_{tt}]
\end{aligned}
\tag{3.4}
$$

$$
\begin{aligned}
\delta r = {}&-\frac{1}{6} + \frac{(r_K - M)^{-1}}{r_K}[C_{tt}h'_{tt} \pm 4(C_{t\phi}h'_{t\phi} \\
&+ 4D_{t\phi}h_{t\phi}) + 4M[(3r_K^2 + a^2)h_t t + h_{\phi\phi}]]
\end{aligned}
\tag{3.5}
$$

The derivatives of the metric components $h'_{\mu\nu}$ depend on the specific metric one chooses. For the deviation in $\gamma_0(r)$, we know that $\gamma_0 \equiv |\kappa_0\Omega_0|$. We already know Ω_0 and now the object of interest is κ_0. To this end we find

$$\kappa_0^2 = \kappa_K^2 = \epsilon(\kappa_{\delta r}^2 + \kappa_h^2) + \mathcal{O}(\epsilon^2) \tag{3.6}$$

In the above expression, $\kappa_{\delta r}^2$ originates due to the shift in the light ring position and κ_h^2 is due to the perturbation metric $h_{\mu\nu}$. Glampedakis et al[12] find these terms as follows and collect them to find the total shift in the Lyapunov exponent:

$$\kappa_{\delta r}^2 = -\frac{24MR_K\delta rM}{r_K^4(r_K - M)^3}\left(\frac{M}{r_K}\right)^{3/2} \tag{3.7}$$

$$\kappa_h^2 = -\frac{4\Delta_K H_K}{r_K^4(r_K - M)^3}\left(\frac{M}{r_K}\right)^{3/2} \tag{3.8}$$

The coefficient R_K is in terms of Kerr M and a and H_K is a function of $h_{\mu\nu}$ and its derivatives. Combining these results, the total post-Kerr κ_0 is

$$\kappa_0 = \kappa_K + \epsilon \frac{\kappa_{\delta r}^2 + \kappa_h^2}{2\kappa_K} \equiv \kappa_K + \epsilon\delta\kappa_0 \tag{3.9}$$

$$\delta\kappa_0 = -\frac{2MN_K}{\sqrt{3}r_K^5\Delta_K}(r_K - M)^{-1} \tag{3.10}$$

The total post-Kerr $\gamma_0(r)$ is then given as follows:

$$\gamma_0 = \kappa_K\Omega_K + \epsilon(\Omega_K\delta\kappa_0 + \kappa_K\delta\Omega_0) \equiv \gamma_K + \epsilon\delta\gamma \tag{3.11}$$

$$\delta\gamma = \mp\frac{4M^2}{\sqrt{3}\Delta_K r_K^5}(r_K + 3M)^{-2}(r_K - M)^{-3}[(r_K + 3M)(G_{tt}h_{tt}'' + G_{\phi\phi}h_{\phi\phi}''$$

$$+ 2Z_{tt}h_{tt}'' + 2Z_{\phi\phi}h_{\phi\phi}'' + 6E_{rr}h_{rr}) \pm (r_K + 3M)\left(\frac{M}{r_K}\right)^{1/2}(G_{t\phi}h_{t\phi}''$$

$$+ 4Z_{t\phi}h_{t\phi}') + 2M(S_{tt}h_{tt} + S_{\phi\phi}h_{\phi\phi} \pm S_{t\phi}h_{t\phi})] \tag{3.12}$$

The reader can find the complete expressions for $R_K, H_K, N_K, E_{rr}, S_{tt}, S_{t\phi}, S_{\phi\phi}$, $Z_{tt}, Z_{t\phi}, Z_{\phi\phi}$ in appendix A.1. The complex template σ we mentioned earlier is now ready. In the eikonal-limit, we associate the real part of the σ with the orbital frequency and the imaginary part with the damping time of the QNM signal so that $\sigma = \sigma_R + \iota\sigma_I$ with

$$\sigma_R = m\Omega_0, \quad \sigma_I = -\frac{|\gamma_0|}{2} \tag{3.13}$$

and knowing Ω_0 and γ_0

$$\sigma_R = m(\Omega_K + \epsilon\delta\Omega) \tag{3.14}$$

$$\sigma_I = -\frac{|\gamma_K + \epsilon\delta\gamma|}{2} \tag{3.15}$$

Having found the post-Kerr eikonal-limit formulae, we can now choose a particular metric and find the new light ring orbital frequency and Lyapunov exponent. We select the Johanssen-Psaltis metric and implement our findings to compute the eikonal limit QNM frequency and then turn our attention to estimating the likelihood of the deviation parameter using GW data.

3.3 Johanssen-Psaltis Metric

$$ds^2 = -[1 + h(r,\theta)](1 - \frac{2Mr}{\Sigma})dt^2 - [1 + h(r,\theta)]\frac{4aMr\sin^2\theta}{\Sigma}dtd\phi$$
$$+ \frac{\Sigma[1 + h(r,\theta)]}{\Delta + a^2\sin^2\theta h(r,\theta)})dr^2 + \Sigma d\theta^2$$
$$+ \left[\sin^2\theta(r^2 + a^2 + \frac{2a^2Mr\sin^2\theta}{\Sigma}) + h(r,\theta)\frac{a^2(\Sigma + 2Mr)\sin^4\theta}{\Sigma}\right]d\phi^2 \quad (3.16)$$

The Johannsen-Psaltis (JP) metric is a parameterization of deviations from the Kerr metric, where the function $h(r,\theta)$ introduces deviations from the Kerr geometry. In its full form, $h(r,\theta)$ is given by

$$h(r,\theta) = \sum_{k=0}^{\infty}(\epsilon_{2k} + \epsilon_{2k+1}\frac{Mr}{\Sigma})\left(\frac{M^2}{\Sigma}\right)^k \quad (3.17)$$

Where the ϵ's are new parameters, in addition to the already existing mass and spin. It was constructed by Tim Johannsen and Dimitrios Psaltis [14] through the Newman-Penrose formalism[15]. It is a still a stationary axisymmetric spacetime but not a vacuum solution to Einstein's Field Equations. This is not a problem for us because we are simply approximating a black hole under a geometry that is not Kerr. The choice of a particular ϵ_3 is made based on the requirements of asymptotic flatness and quadrupole moment. Asymptotic flatness requires that $\epsilon_0 = \epsilon_1 = 0$ and $|\epsilon_2| \leq 4.6x10^{-4}$ is constrained by the Lunar Ranging Experiment[16]. ϵ_3 corresponds to a deformation in the Kerr quadrupole formula[12] such that

$$Q_{JP} = Q_{Kerr} + \epsilon_3 M^3 \quad (3.18)$$

Hence in our analysis we limit ourselves to constraining ϵ_3 using ringdown data available from GW events. There has been a study[17] of black hole accretion disk thermal spectra that find $\epsilon_3 \leq 5$. It is generally assumed that ϵ_3 takes values of order $\mathcal{O}(10)$ and it is interesting to see how GW affect this parameter. All ϵ_k's, where $k > 2$, can be considered for analysis. Since ϵ_3 is the next non-zero parameter after ϵ_2 and other attempts have been made to constrain it, we will try and constrain it with gravitational wave data. We drop the higher ϵ's by setting $\epsilon_k = 0$

for $k > 3$.

For the specific case of ϵ_3, $h(r, \theta)$ takes the form:

$$h(r, \theta) = \epsilon_3 \frac{M^3 r}{\Sigma^2} \tag{3.19}$$

Furthermore, we only consider the equatorial orbits to make our life easier and set $\theta = \frac{\pi}{2}$. All results found in this text are only valid for equatorial orbits. As we saw in figure 2.2, one can imagine 3D-equivalents (the hypersurface (r, θ, ϕ), at some time t) of Kerr and JP spacetimes.
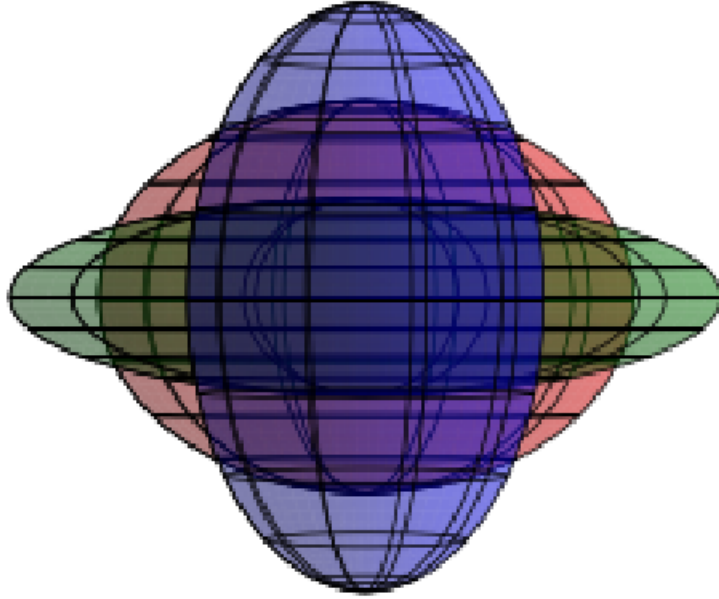

Figure 3.1: Ergospheres of Kerr and JP spacetime for a visual representation of how ϵ_3 affects the geometric structure of the black hole. $\epsilon_3 = 0$ would correspond to a Kerr black hole. For the JP spacetime, when $\epsilon_3 > 0$ the ergosphere would become more prolate and when $\epsilon_3 < 0$ it would be more oblate. This change in the structure of the ergosphere causes the physical observables to be different relative to Kerr. The purpose of this figure is purely illustrative for arbitrary, non-zero ϵ_3.

Having established the development of the JP metric, let us now turn our attention back to finding the orbital frequency and Lyapunov exponent in this set up. Assuming that deviations from Kerr are small and keeping only up to linear order in ϵ_3, we can really see the structure $g_{\mu\nu}^{JP} = g_{\mu\nu}^{K} + \epsilon h_{\mu\nu}^{JP}$.:

$$g_{tt}^{JP} = -(1 - \frac{2Mr}{\Sigma}) - \epsilon_3 \frac{M^3(r - 2M)}{r^4} \tag{3.20}$$

$$g_{rr}^{JP} = \frac{\Sigma}{\Delta} + \epsilon_3 \frac{M^3(r - 2M)}{\Delta^2} \tag{3.21}$$

$$g_{\theta\theta}^{JP} = \Sigma \tag{3.22}$$

$$g_{\phi\phi}^{JP} = (r^2 + a^2 \frac{2Ma^2 r \sin^2\theta}{\Sigma}) \sin^2\theta + \epsilon_3 \frac{a^2 M^3(r + 2M)}{r^3} \tag{3.23}$$

$$g_{t\phi}^{JP} = -\frac{2Mar \sin^2\theta}{\Sigma} - \epsilon_3 \frac{2aM^4}{r^4} \tag{3.24}$$

where Σ and Δ are the usual Kerr functions.

Using this metric for the recipe described in the previous section, we set out to finding the light ring properties for finding an eikonal limit QNM formula. The first object we need is the modified light ring position, which we obtain by demanding that the potential and its derivative must vanish for an orbit to be circular. In the JP geometry, this condition leads to the following expressions:

$$V'_{eff}(r) = (\epsilon_3 M^3 + 4r^3)(a^2 - b^2) + 6Mr^2(a - b)^2 + 6r^5 = 0 \tag{3.25}$$

$$V_{eff}(r) = (\epsilon_3 M^3 + 4r^3)[2M(a - b)^2 + r(a^2 - b^2)] + r^6 = 0 \tag{3.26}$$

This system of equations is not exactly solvable but we can assume small perturbations around the Kerr metric and consider an expansion in ϵ_3 to look for an approximate solution. With the following ansatz:

$$r_0 = r_K + \delta r_1 \epsilon_3 + \delta r_2 \epsilon_3^2 + \dots \tag{3.27}$$

$$b_0 = b_k + \delta b_1 \epsilon_3 + \delta b_2 \epsilon_3^2 + \dots \tag{3.28}$$

solving order by order in ϵ_3 to obtain:

$$\Omega_0 = \frac{1}{b_K} - \frac{2\delta b_1}{b_K^2} \epsilon_3 + \mathcal{O}(\epsilon_3^2) \tag{3.29}$$

$$\gamma_0 = \gamma_K + \delta\gamma_1 \epsilon_3 \tag{3.30}$$

38

The terms corresponding to the deviations, $\delta r_1, \delta b_1$ and $\delta\gamma_1$ are provided in appendix A.3.

Since we are assuming that the expansion parameter ϵ_3 is small, we only keep leading order terms in the orbital frequency and Lyapunov exponent. We use equations 3.29 and 3.30 in equation 3.14 and 3.15 respectively to find the eikonal-limit QNM spectrum. Figures 2 and 3 produced by Glampedakis et al.[12] show the trends in the light ring position, orbital frequency and the Lyapunov exponent for different values of ϵ_3.
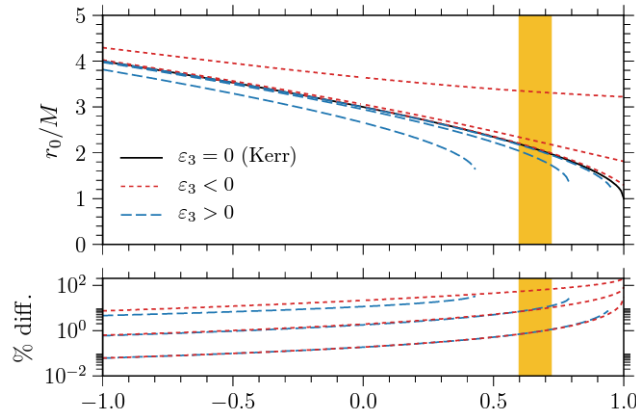

Figure 3.2: The light ring radius r_0 in JP. The yellow band represents the measured spin of $a = 0.67^{0.05}_{0.07}M$[8] of the event GW150914. This plot shows the deviation from the Kerr light ring due to $|\epsilon_3| = 0.1,\ 1,\ 10$. The bottom panel shows the relative difference between between JP and Kerr light rings. Figure from [12].
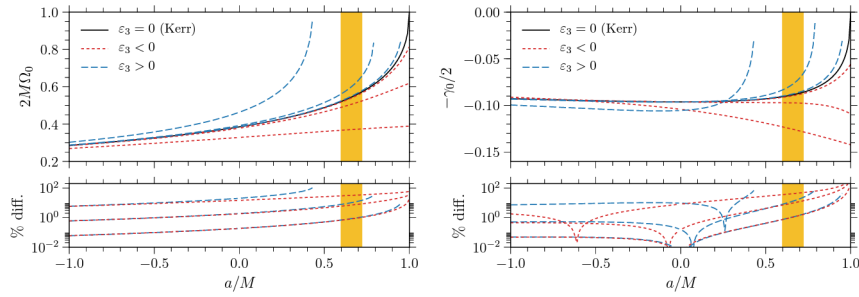

Figure 3.3: Orbital frequency and Lyapunov exponent for the same values of $|\epsilon_3|$. The bottom panel shows the relative difference between between JP and Kerr orbital frequency and Lyapunov exponent.[12]

39

In another paper[18], Carson and Yagi find equivalent and more pleasing-to-the-eye results

$$\sigma_R = \sigma_R^K + \epsilon_3 \left(\frac{1}{81\sqrt{3}M} + \frac{10}{729M}\chi + \frac{47}{1458\sqrt{3}M}\chi^2 \right) \qquad (3.31)$$

$$\sigma_I = \sigma_I^K - \epsilon_3 \left(\frac{1}{486M}\chi + \frac{16}{2187\sqrt{3}M} \right) \qquad (3.32)$$

We will use these expressions for the results produced by Python scripts in the next chapter.

Chapter 4

Ringdown Analysis

The first task is to prepare the data so that it does not know anything about Kerr, an agnostic data file if you will. This is produced by fitting damped sinusoids to the actual data and this task was performed by Dr. Shilpa Kastha of the Strong Team at NBI, Copenhagen. Now that we have an agnostic data file, we can perform computational tasks on the data to find the likelihood of parameters. The algorithm used by the Python script is outlined as follows:

- Import the necessary packages

- Read the relevant data file

- Define Python functions for computing the frequency and damping times, provided some combination of (M, χ, ϵ_3)

- Invert the frequency and damping time functions to find a value of M for each function temp and Temp, respectively.

- Check if the absolute difference between temp and Temp is less than 0.001

- Loop over the ranges of χ and ϵ_3 and use the mass value, temp, in combination with each value of χ and ϵ_3 to produce the frequency and damping time for each combination

- Check if the absolute difference between computed frequency (damping time) and data frequency (damping time) is within 0.0001.

- Convert values to SI units

- Register computed frequency, damping time, M, χ and ϵ_3

- Produce scatter plots

- Produce contour plots and 1D histograms

The Python script for implementing the described algorithm is available on the author's GitHub repository [19].

4.1 GW150914

LIGO's first ever observed gravitational wave event is GW150914 and it is truly a huge milestone in scientific research. Some properties of the event are tabulated below. We will use openly available LIGO data and assume that the perturbed black hole in the ringdown is described by the JP metric, in order to find constraints on the deviation parameter ϵ_3.

Focusing on the 220 mode ($l = m = 2$, $n = 0$), first we produce frequency-damping time distributions by choosing ϵ_3 discretely and plot them on top of each other to see how the distribution changes.
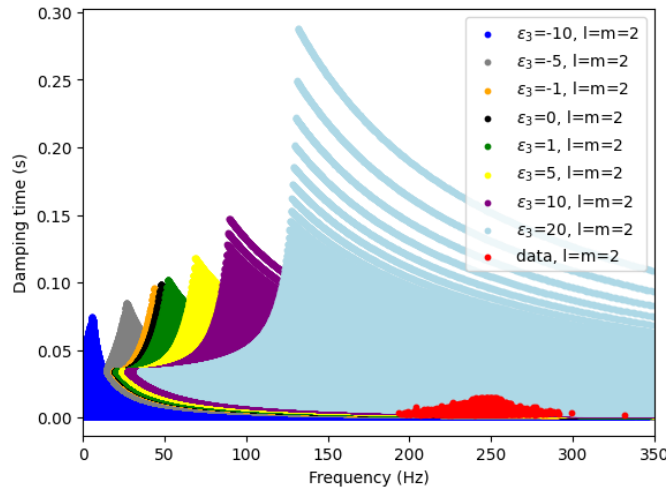

Figure 4.1: Frequency-damping time distribution. The general features of the distribution remain the same, except that the distribution shrinks ($\epsilon_3 < 0$) or expands($\epsilon_3 > 0$).

One can clearly see that the overlap of the data points with the produced values is much greater for $\epsilon_3 > 0$ and for $\epsilon_3 < 0$ the produced distribution starts to leave the data points region for more and more negative values. We use this observation to predict that when the algorithm described earlier is implemented, the output for the ϵ_3 will favour more positive values than negative values. Let us now look at the mass-spin distribution and since we already know about the Kerr mass and spin of the black hole, we can once again discretely choose ϵ_3 to see how the mass-spin distribution is affected by non-zero ϵ_3.
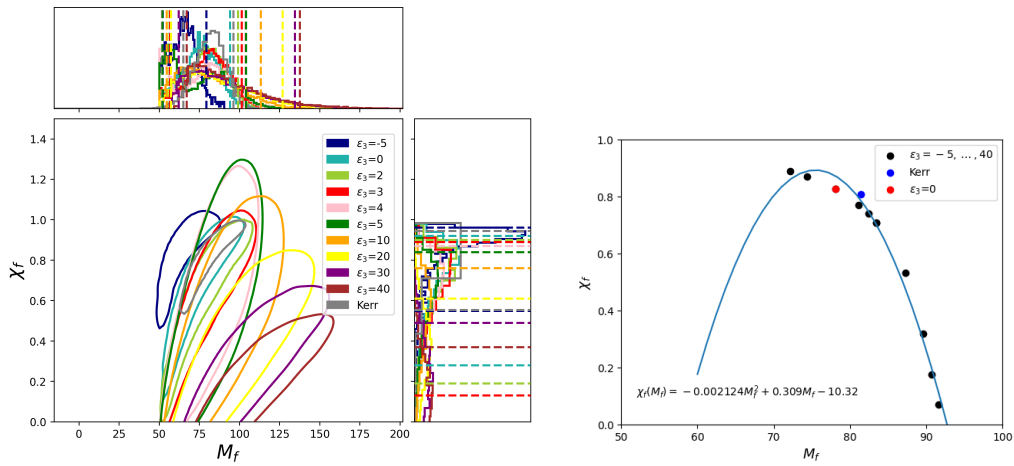
(a) Change in the 90% contours of the mass-spin distributions due to non-zero ϵ_3, given the data for GW150914.

(b) Quadratic curve fit to track the trajectory of the mass-spin distribution (left) as ϵ_3 changes from -5 to 40. The dots represent the mass and spin value for each ϵ_3, computed for a single value of frequency and damping time from the data.

Figure 4.2: GW150914: Mass-spin distributions for discrete values of ϵ_3

Combining all of the information we have gathered and discussed and running the Python script for the GW150914 agnostic data file, we can produce corner plots that show the correlations between each pair of the parameter space. First we check by considering the parameter ranges to be $M = [20, 200]$, $\chi = [0, 1]$ and a smaller range of $\epsilon_3 = [-1, 1]$, so that we can see how the non-zero but small ϵ_3 affects the mass-spin distribution but does not deviate too much. After all, we

have assumed small perturbations around the Kerr metric in our theoretical set up.
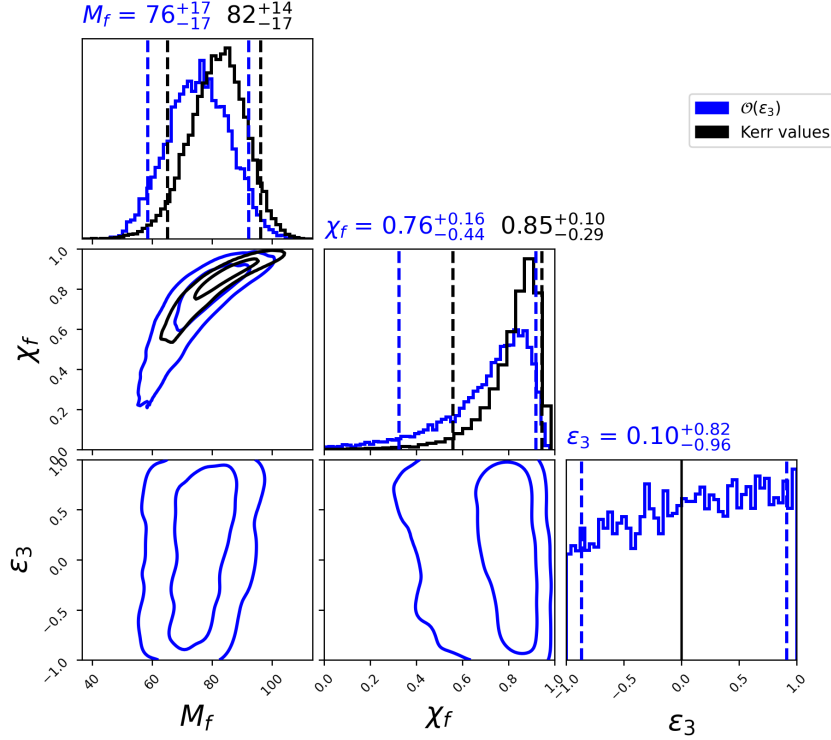

Figure 4.3: GW150914: Posteriors obtained by running the Python script with parameter ranges $M = [20, 200]$, $\chi = [0, 1]$ and $\epsilon_3 = [-1, 1]$. Kerr values of M and χ are also shown for comparison. The ϵ_3 posteriors are almost flat, meaning that there is still room for larger ϵ_3's that can satisfy equation 3.31, 3.32 suggesting that a larger range of ϵ_3 should be considered.

We increase the range of ϵ_3 while keeping the ranges of M and χ the same and run the same script to see if we observe the expected changes.
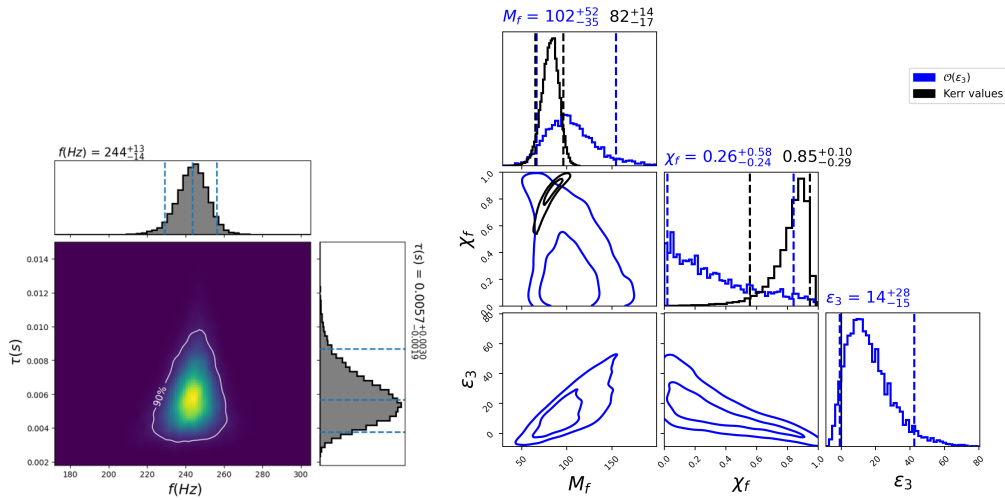
(a) 220 mode data from GW190521 used to produce the plot on the right.

(b) GW150914: Corner plot showing the posteriors for M, χ and ϵ_3. These values are produced by inverting the expressions 3.31, 3.32 and using the data shown on the left.

Figure 4.4: Using GW150914 data to estimate the posterior for ϵ_3

With a larger range on ϵ_3, the posterior is no longer flat and we see that the distribution is slightly skewed and favoring $\epsilon_3 > 0$. The features of the contours can already be predicted just by staring at equation 3.31. The non-Kerr term in equation 3.31 needs to be small and so higher values of ϵ_3 are compensated by higher values of M and lower values of χ and vice versa. This result is consistent with the expectations of the algorithm.

While working on this project, there was a paper by Dey et al.[20] where they perform the same task but with a different Python package, PyRing[21], and produce the likelihoods of two geometries; the Johanssen-Psaltis metric and the Manko-Novikov metric. The authors were contacted to ask for the posterior data they produce with their analysis and they were happy share their work. Figure 4.5 shows the comparison between the two analyses. One key difference is that they do not use the post-Kerr approximation formulae and consider the JP metric in its full form, as they mention in their paper[20], leading to the difference in the posterior distributions. The similarity between the two posteriors is that the general structure of the contours depicts the same trend that is predicted by

equation 3.31. Additionally, both approaches indicate that the data is supported by $\epsilon_3 > 0$ values.
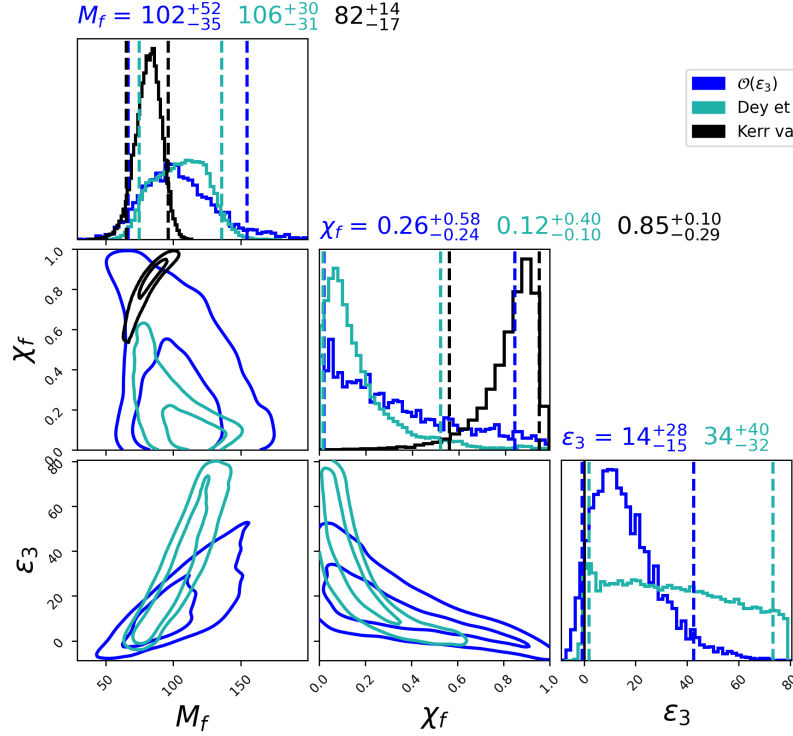

Figure 4.5: GW150914: Comparative results between this work and Dey et al.[20]. The general structure of the contours are similar but the sharpness of features is different due to the difference in the two approaches.

4.2 GW190521

The analysis performed on GW150914 data can be applied to any GW event with appropriate prior ranges. This section addresses the case of GW190521 where we swap the GW150914 agnostic data file with GW190521 agnostic data file. GW190521 is important and interesting because, as shown by Capano et al.[3], it has another excited mode in the ringdown. We have already seen this result in the figure 1.2. The community agrees on the existence of the 220 mode and it is generally believed that other modes are too weak to be seen in the ringdown signal. Capano et al. show that the 330 mode is in fact visible in GW190521 and also provide a

statistical validation of their methods[22].

Since we have already seen the 220 mode results for GW150941, we go through the same steps for the 220 mode of GW190521 first and then the code can be modified to incorporate the 330 mode as well. Figure 4.6 shows the mass-spin distribution and its trajectory as the value of ϵ_3 changes discretely. Notice that the separation between the contours is larger than in figure 4.2. This means that GW190521 is more sensitive to the change in ϵ_3 and also that the expressions 3.31 and 3.32, given the data, will not allow ϵ_3 to be as large as it turns out to be in the case of GW150914. This happens due to the fact that GW190521 is better measured and the errors in the measurement are smaller compared to GW150914.
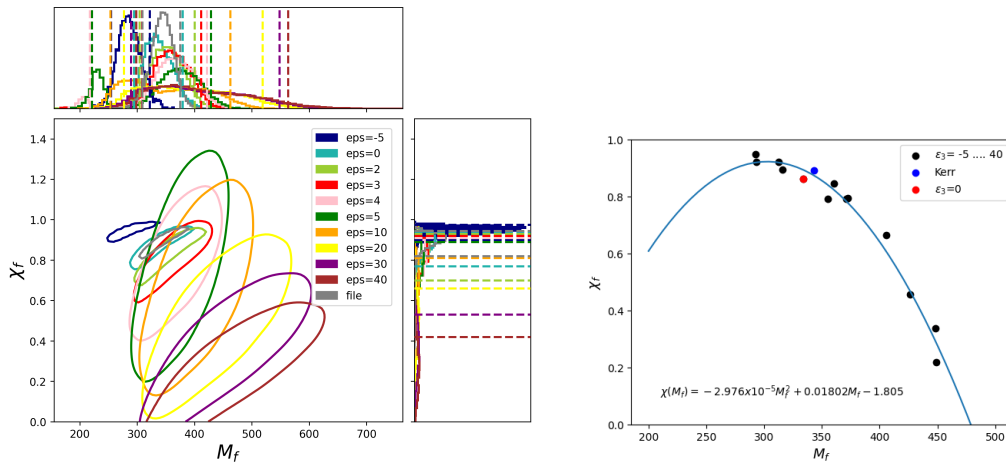
(a) Change in the 90% contours of the mass-spin distributions due to non-zero ϵ_3, given the data for GW190521. Note that the distribution is more sensitive to change in ϵ_3 compared to the GW150914 distributions.

(b) Quadratic curve fit to track the trajectory of the mass-spin distribution (left) as ϵ_3 changes from -5 to 40. The dots represent the mass and spin value for each ϵ_3, computed for a single value of frequency and damping time from the data.

Figure 4.6: GW190521: Mass-spin distributions for discrete values of ϵ_3

It is already known from GW150914 analysis that the upper bound on $\epsilon_3 \gg 1$ and the Kerr mass for GW190521 is around $300 M_0$, therefore the prior ranges for the parameters are adjusted to be; $M = [200, 600]$, $\chi = [0, 1]$ and $\epsilon_3 = [-30, 100]$. The range for ϵ_3 is kept the same to maintain the agnostic approach toward this

parameter. Running the code for this configuration and of course the relevant data file for GW190521, it is clear that using GW190521 gives a better constraint on ϵ_3.
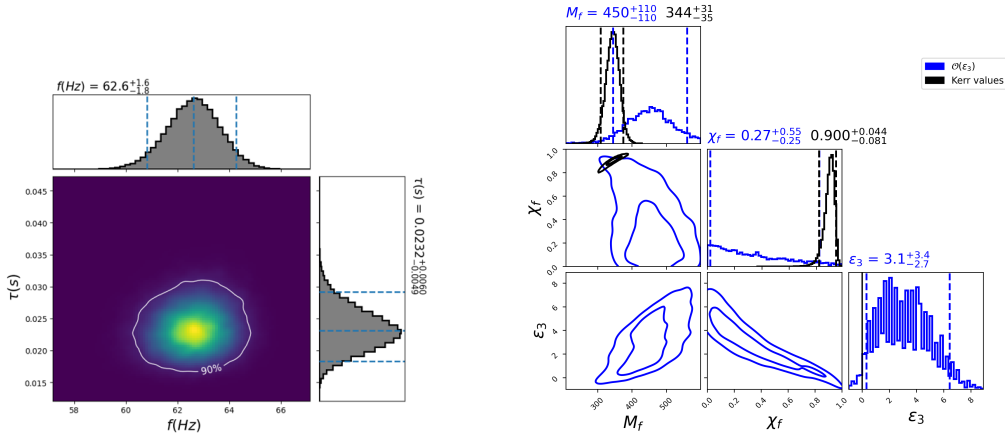
(a) 220 mode data from GW190521 used to produce the plot on the right.

(b) GW190521:Corner plot showing the posteriors for M, χ and ϵ_3. These values are produced using by inverting the expressions 3.31, 3.32 and 220 mode data only. Since the measurement of the ringdown is much better compared to GW150914, this event allows for a better measurement of ϵ_3.

Figure 4.7: Using GW190521 to estimate the posterior for ϵ_3.

Figure 4.8 is a comparison between the values of ϵ_3 we find using the two events. Even with just considering the 220 mode, the improvement in the constraint on ϵ_3 is clearly visible and thus GW190521 is in fact a better candidate for analysis, compared to GW150914. This constraint is expected to get tighter when the 330 mode is also included in the analysis.
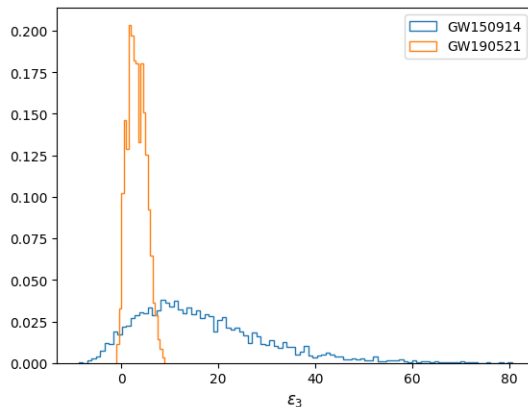
Figure 4.8: Comparison of ϵ_3 posterior for the two events GW150914 and GW190521

Now to include the additional information provided by the 330 mode, we can modify our code to consistently add the 330 mode and perform the same task to produce the following posteriors. An important detail about the relation between the 220 and 330 modes is that the real part of the two QNM frequencies are related by a ratio:

$$\omega_R^{330} = \frac{3}{2}\omega_R^{220} \tag{4.1}$$

This means that the 330 mode is not some entirely new information but a supporting piece for the 220 mode. Consequently, improving our knowledge about the 220 mode, in a sense, further reducing the errors. This task is intentionally left to be performed with PyCBC inference.

4.3 PyCBC

We now move on to perform the analysis in a more formal way by including the statistical method, Bayesian inference, by using PyCBC. PyCBC is a software package used to explore astrophysical sources of gravitational waves. It contains algorithms that can detect coalescing compact binaries and measure the astrophysical parameters of detected sources. PyCBC was used in the first direct detection of gravitational waves by LIGO and is used in the ongoing analysis of LIGO and

Virgo data. PyCBC was featured in Physics World as a good example of a large collaboration publishing its research products, including its software.[23]

It has been used in the closing phase of this thesis for more formal results where the package uses Bayesian inference to look for posteriors given a particular event.The 'CBC' in PyCBC stands for compact binary coalescence and is used for Kerr black hole spectroscopy where it uses Kerr predictions to compute a QNM spectrum and then fits it available data. Given a set of priors on the parameters, it produces GW waveforms of the form

$$h_+ + \iota h_X = \frac{M}{r} \sum_{lmn} A_{lmn} e^{\iota(\omega_{lmn} t + \phi_{lmn})} e^{-t/\tau_{lmn}} S_{lmn} \tag{4.2}$$

Where the S_{lmn} are the spheroidal functions evaluated at the QNM frequencies[13]. The relevant pieces of the above expression that we need are the ω_{lmn} and τ_{lmn}.

PyCBC maps $(M, \chi) \longrightarrow (\omega, \tau)$ by using the following dimensionless frequency and quality factor expressions obtained by Berti et al.[13]:

$$F_{lmn} = f_1 + f_2(1 - \chi)^{f_3} \tag{4.3}$$

$$Q_{lmn} = q_1 + q_2(1 - \chi)^{q_3} = \frac{\omega_{lmn} \tau_{lmn}}{2} \tag{4.4}$$

where the fitting coefficients f_1, f_2, f_3, q_1, q_2, and q_3 are obtained by numerical fits.

m	n	f_1	f_2	f_3	%	q_1	q_2	q_3	%
2	0	1.5251	−1.1568	0.1292	1.85	0.7000	1.4187	−0.4990	0.88
	1	1.3673	−1.0260	0.1628	1.56	0.1000	0.5436	−0.4731	1.69
	2	1.3223	−1.0257	0.1860	1.91	−0.1000	0.4206	−0.4256	2.52
1	0	0.6000	−0.2339	0.4175	2.03	−0.3000	2.3561	−0.2277	3.65
	1	0.5800	−0.2416	0.4708	2.40	−0.3300	0.9501	−0.2072	3.18
	2	0.5660	−0.2740	0.4960	4.04	−0.1000	0.4173	−0.2774	2.46
0	0	0.4437	−0.0739	0.3350	1.04	4.0000	−1.9550	0.1420	2.63
	1	0.4185	−0.0768	0.4355	1.50	1.2500	−0.6359	0.1614	4.01
	2	0.3734	−0.0794	0.6306	2.72	0.5600	−0.2589	0.3034	4.33
−1	0	0.3441	0.0293	2.0010	0.07	2.0000	0.1078	5.0069	2.82
	1	0.3165	0.0301	2.3415	0.05	0.6100	0.0276	13.1683	0.67
	2	0.2696	0.0315	2.7755	0.43	0.2900	0.0276	6.4715	2.40
−2	0	0.2938	0.0782	1.3546	0.63	1.6700	0.4192	1.4700	0.71
	1	0.2528	0.0921	1.3344	0.87	0.4550	0.1729	1.3617	0.79
	2	0.1873	0.1117	1.3322	1.34	0.1850	0.1266	1.3661	1.16

Figure 4.9: Fitting coefficients tabulated for the $l = m = 2$ mode. A similar routine is used to produce coefficients of higher modes, $l > 2$.

For a given value of l, m, and n, the built-in Python function get_lm_f0tau in

the module "conversions.py" converts a given (M, χ) to (ω, τ) and then the function get_lm_f0tau_allmodes produces values for all possible modes supported by PyCBC. Once a value of (ω, τ), the code moves ahead and uses this value in the "ringdown.py" module to produce damped sinusoids by passing the values to the function td_damped_sinusoid which produces the h_+ and h_X polarization. And then the function multimode_base, in the same module, sets up this damped sinusoid for further processing by taking an 'approximant' as an argument which specifies the parameters to be used and the output that will be generated. As soon as a waveform is successfully generated, then the code moves onto match-filtering where the all of the statistics comes in. As the name implies, produced-waveforms are matched with the data-waveforms and the parameters for which there is a match, are registered. This is accomplished by sampling through the parameter space. In ringdown analysis, the usual sampler of choice is Dynesty. Running inference for a particular event with appropriate priors on the parameters, spits out the posteriors given the data.

The previous paragraph outlines the routine followed by PyCBC but specifically for Kerr. Since we are now dealing with a new geometry, the parameter space is different and therefore the QNM spectrum is different. We must consistently alter the relevant source code to accommodate the new parameter, ϵ_3 introduced by the JP metric, so that we can produce waveforms due to the new geometry. The mapping to be done is $(M, \chi, \epsilon_3) \longrightarrow (\omega, \tau)$, using equation 3.31 and 3.32 or equations 3.29 and 3.30, since they are equivalent. The author successfully introduced these new expression in the source code and modified the sinusoid-producing functions.

TABLE II Summary of all the changes made to the source code and can be viewed in detail in the author's PyCBC GitHub repository[19].

Kerr	Johanssen-Psaltis
get_lm_fotau	get_JP_lm_fotau
get_lm_fotau_allmodes	get_JP_lm_fotau_allmodes
mass_spin_required_args	mass_spin_eps_required_args
multimode_base	multimode_base (with ϵ_3)
get_td_from_final_mass_spin	get_td_from_final_mass_spin_eps
TdQNMfromFinalMassSpin	TdQNMfromFinalMassSpinEps
select_waveform_generator	additional conditions for ϵ_3
TDomainMassSpinRingdownGenerator	TDomainMassSpinEpsRingdownGenerator

One important output was to plot the waveform using the newly defined functions and check the if limiting case, where $\epsilon_3 = 0$, gives the same waveform as Kerr. Figure 4.10 shows this comparison and figure 4.11 shows different waveforms due to different values of ϵ_3.
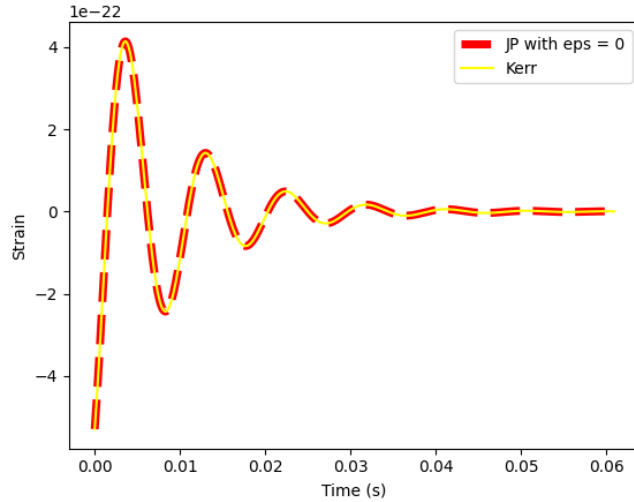

Figure 4.10: Waveforms produced by using the functions ringdown.get_td_from_mass_spin_eps and ringdown.get_td_from_mass_spin for the JP and Kerr geometries, respectively.
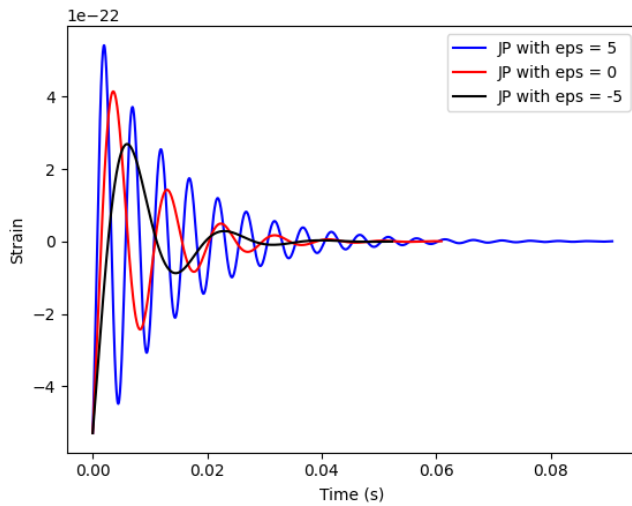
Figure   4.11:   Waveforms   produce   by   using   the   function
ringdown.get_td_from_mass_spin_eps with $\epsilon_3 = -5,\ 0,\ 5$.

Having successfully produced the waveform, the next step is to run the full
inference and analyze the output. We already have some idea from the Python
script outputs and so we expect PyCBC results to be along the same lines. The
syntax and configuration files can be found in the author's GitHub repository[19].
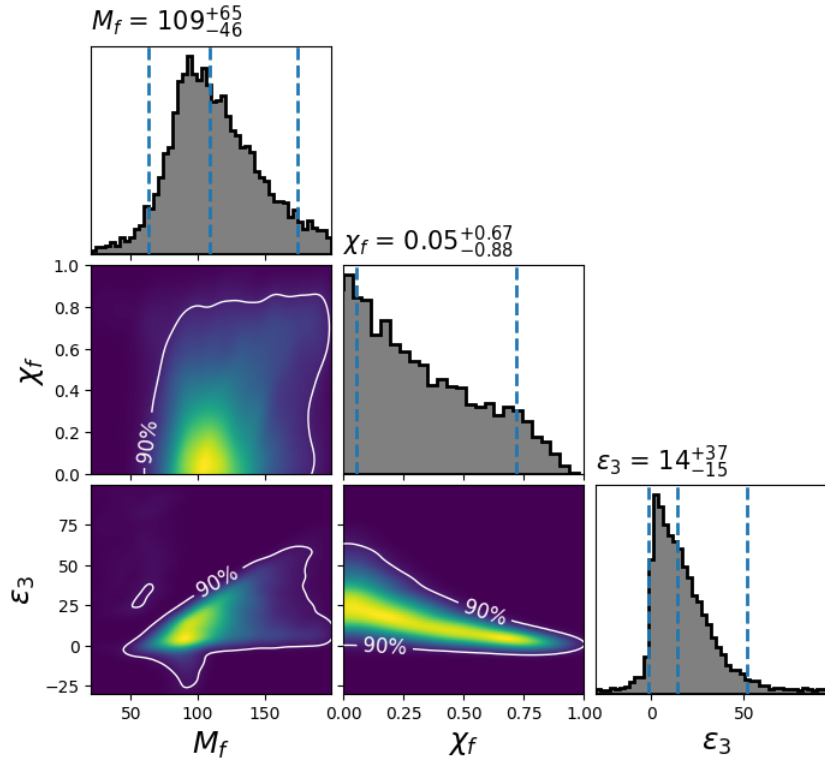
Figure 4.12: Posterior distributions obtained by running inference for GW150914.

Figure 4.12 shows the output of the inference run for GW150914 and we see that is not quite the same as what we saw in the Python script output. There are some similarities such as the ϵ_3 posterior here is still favouring more positive values and trailing off after 50, the M_f and χ_f are also somewhat in the same range as the previous result. Some refinement is still needed in terms of the mapping and the expressions used for mapping and it must be noted that the inference runs are still a work in progress and some refinement is still needed. The features of figure 4.4 are expected to be reproduced and more defined once the PyCBC issues are resolved and this task is marked for follow up work after submission of this document.

Chapter 5

Discussion

The first point to keep in mind is that the post-Kerr approximation we make by using the Johanssen-Psaltis metric is through a truncated metric where the assumption is that ϵ_3 is small enough so that only linear order terms are kept and also the Kerr metric must be reproduced in the limit where $\epsilon_3 \longrightarrow 0$. This is easily checked by taking the limit of the expressions we wrote for the JP metric 3.20-3.24. The requirement of ϵ_3 being small is still a concern which is alarming at first sight because the measurement we make on the parameter are $\gg 1$ in both cases, sections 4.1 and 4.2.

For GW150914, we see that $\epsilon_3 = 14^{28}_{-15}$. For GW190521, it is more tightly constrained near zero, $\epsilon_3 = 3.1^{3.4}_{-2.7}$. Both of these are consistent with $\epsilon_3 = 0$ as shown in the mass-spin distributions (figures 4.2 and 4.6) as well as the 1D histograms for ϵ_3 in figures 4.4 and 4.7. The GW190521 constraint is better because it is closer to being 'small' compared with the GW150914 result. Although we have not included the 330 mode from GW190521 in this analysis, this measurement is expected to be even better because we have access to a larger data set if the 330 mode of a ringdown is observed. Therefore, we can reduce the error bars on the measurement of ϵ_3 and may even be able to get closer to $\epsilon_3 \sim 1$. This is a predictive result and future work could examine what further constraints can be obtained by including the 330 mode.The analysis performed with PyCBC inference (4.12) is also a validation of our Python script results (4.4). Meaning that whatever we did in our Python script was on the right track. There are some differences such as the $M - \chi$ contours are different for the two approaches. However, the values on the 1D histograms are still similar.

The differences in the results between this work and Dey et al.'s (figure 4.5) are due to the difference in the calculation of the frequency and damping time expressions, as they mention in their paper[20].We have used a truncated JP metric whereas Dey et al. do not use this approach and keep the JP metric intact throughout. Due to this difference in calculation methods, our ϵ_3 is not the same as Dey et al.'s ϵ_3. Ours is a perturbative parameter whereas theirs is a more 'pure' ϵ_3. It must be noted that this differences affect more the sharpness of the features in the 90% contours of the corner plots and the posteriors we find are still within the same ballpark values.

We turn our attention to the largeness of ϵ_3 in our results. Since this is a perturbative calculation, the expectation would be that $\epsilon_3 \ll 1$ because that is the assumption we make while making the expansion and also when dropping higher order terms because they would be too small to be significant. The higher order terms are essential error-reducing quantities that help control the measurements. Our ϵ_3 is much larger than 1 and therefore it would not make sense to incorporate higher order terms in our analysis. What we are interested in, is not so much constraining ϵ_3, but rather finding cases where the Kerr assumption is violated. As such we are looking for anomalies, not quantitative precision measurements of deviation parameters. This is particularly true in the JP metric, where ϵ_3 is only one of an infinite number of parameters. One wouldn't expect all the other parameters to be zero in a general modified theory anyway, so assuming they are zero is as artificial as truncating the Taylor expansion when converting to frequency and damping time.

Our methods can be extended to more complicated situations. An example would be the case where we allow higher ϵ_k where $k > 3$ and find the light ring properties.As we have already seen with the modified-Kerr case (section 2.6), a deformation of the metric that is dependent on radial coordinate necessarily changes the light ring position and consequently, the orbital frequency and damping times. Let's assume that now we have two non-zero ϵ's, ϵ_3 and ϵ_4. We already have results pertaining to ϵ_3 but since ϵ_4 has it's own radial dependence, the final expressions for the QNM spectrum may have an interplay of these two parameters. Now, there will be a space of four parameters, $(M, \chi, \epsilon_3, \epsilon_4)$ instead of the three-dimensional one we have been handling, (M, χ, ϵ_3). The frequency and damping time templates produced with these four may be completely different but still useful to find constraints on ϵ_3 and ϵ_4. In this scenario, the constraints

on ϵ_3 shown in figure 4.8 will be different due to the presence of non-zero ϵ_4. However, this is simply a matter of motivation and time required to perform this calculation. Additionally, including more and more parameters also raises the issue of trying to fit too many parameters with just two numbers, frequency and damping time.

Carson and Yagi [18] perform an analysis for GW150914-like events but not with ringdown data from LIGO. They use future technologies and also include the inspiral phase of the binary. We have not addressed the inspiral or future detectors anywhere in this work because we are only limiting ourselves to ringdown analysis and LIGO data. They perform the IMR (Inspiral-Merger-Ringdown) analysis which means they are including more information about an event and therefore will have better constraints. On top of additional information, they also consider future technology like LISA and Cosmic Explorer for their predictions. Table 5.1 summarizes their finding and predictions.

		ϵ_3 (JP [37])		β (mod.-Δ [40,59])	
		IMR	Parametrized	IMR	Parametrized
O2 [4]	GW150914 [5]	$(7)^a$	$(5)^a$	$(2)^a$	$(1)^a$
	GW170729 [80]	$(10)^a$	$(14)^a$	$(14)^a$	$(11)^a$
CE [19]	GW150914 [5]	0.05	0.05	0.05	0.02
	GW170729 [80]	0.6	0.5	0.06	0.07
CE + LISA [19,21]	GW150914 [5]	0.02	0.03	5×10^{-3}	4×10^{-3}
	GW170729 [80]	0.05	0.09	0.05	0.03
LISA [21]	EMRI	$(2 \times 10^{-3})^b$	10^{-3}	$(2 \times 10^{-4})^b$	10^{-4}
	SMBHB	0.02	0.01	10^{-3}	10^{-3}

[a]Constraints with the aLIGO O2 detector are not as reliable because they fall beyond the small-deviation approximation made when deriving ppE parameters.
[b]Constraints from EMRIs with IMR consistency tests may not be accurate since the IMRPhenomD waveforms were calibrated to numerical relativity simulations with mass ratios only up to $1:18$. In the parametrized test, all such numerical relativity (NR) fits have been removed and integrations stopped before the merger to avoid such inaccuracies.

Figure 5.1: This is a snip from the paper [18] the text under the table elaborates why LIGO is not reliable for constraining ϵ_3. They also do the same analysis another parameter, β, due to some other metric. Note that even with IMR results the estimated value of ϵ_3 is still larger than 1 for GW150914.

This implies that the analysis we have performed is a chunk of the larger analysis that can be performed. Our ringdown-only results ($\epsilon_3 = 14^{28}_{-15}$) are still reasonable compared to the IMR results shown in 5.1 where $\epsilon_3 = 7$ from the O2 run. Furthermore, the GW190521 posteriors are already better than GW150914.

The post-Kerr approximation as described in chapter 3, in the sense that we write the some axisymmetric metric in a form which is $g^K_{\mu\nu} + \epsilon h_{\mu\nu}$. It is only a

deformation to the metric but useful in understanding non-GR scenarios. . In a modified theory of gravity, one writes the action and looks for black hole solutions. For example, the action of an Effective Field Theory extension of GR[24] has the following structure:

$$\mathcal{S}_{eff} = \int dx^4 \sqrt{-g} 2 M_{pl}^2 \left(R - \frac{\mathcal{C}^2}{\Lambda^6} - \frac{\tilde{\mathcal{C}}^2}{\tilde{\Lambda}^6} - \frac{\mathcal{C}\tilde{\mathcal{C}}}{\Lambda_-^6} \right) \tag{5.1}$$

where $\mathcal{C} = R_{\mu\nu\alpha\beta}R^{\mu\nu\alpha\beta}$ and and $\tilde{\mathcal{C}} = R_{\mu\nu\alpha\beta}R^{\tilde{\mu\nu}\alpha\beta}$. The QNM spectrum for the case of non-spinning[24] black holes as well as spinning[25] black holes in this theory have been calculated but not yet been constrained with observational data. The methods used in this research can be extended provided that we have the QNM spectrum of the theory we are interested in.

Chapter 6

Conclusions

This thesis considers the JP metric as a first step toward beyond-GR theories and attempts to find constraints on non-Kerr parameters. We have found a tighter constraint on the ϵ_3 parameter compared to existing constraints. Figure 4.7 shows that $\epsilon_3 = 3.1^{3.4}_{-2.7}$ at 2σ using the 220 mode of GW190521 ringdown. It is expected to get get even smaller if the 330 mode is also included in the analysis. Our constraint is tighter compared to existing constraints from GW150914 ($\epsilon_3 = 34^{40}_{-32}$)[20] and from the accretion disk thermal spectral where $\epsilon_3 \leq 5$[17]. Our constraint is obtained by using the truncated metric expressions for frequency and damping time and the analysis is consistent when implemented for the two events, GW10914 and GW190521, independently. Thereafter, the constraints obtained by the procedure adopted by Dey et al. is implemented on GW190521 will also be tighter than GW150914.

The JP metric is a simple and useful stepping stone leading to non-Kerr parameter estimation. We see that with LIGO ringdown data that ϵ_3 is not within our assumption that $\epsilon_3 \ll 1$. The GW190521 constraint is closer to this assumption than GW150914. Nonetheless, the task is useful in measuring non-Kerr parameters with future technologies like LISA and Cosmic Explorer and the parameters are expected to be constrained better.

The primary objective of this text is to report the results of the research. We check for deviations from the Kerr geometry by using the GW190521 observation, since the ringdown data is much better than GW150914 and has additional information because of the 330 mode presence.

Bibliography

[1] Event Horizon Telescope. Sagitarius A*. [Online]. Available: https://eventhorizontelescope.org/blog/astronomers-reveal-first-image-black-hole-heart-our-galaxy

[2] LIGO Scientific Collaboration. Gravitational Waves and Sources. https://www.ligo.caltech.edu/page/what-are-gw,https://www.ligo.caltech.edu/page/gw-sources.

[3] C. D. Capano, M. Cabero, J. Westerweck, J. Abedi, S. Kastha, A. H. Nitz, Y.-F. Wang, A. B. Nielsen, and B. Krishnan, "Observation of a multimode quasi-normal spectrum from a perturbed black hole," 2021. [Online]. Available: https://arxiv.org/abs/2105.05238

[4] K. Yagi, "Analytic estimates of quasi-normal mode frequencies for black holes in general relativity and beyond," 2022. [Online]. Available: https://arxiv.org/abs/2201.06186

[5] T. Regge and J. A. Wheeler, "Stability of a schwarzschild singularity," *Phys. Rev.*, vol. 108, pp. 1063–1069, Nov 1957. [Online]. Available: https://link.aps.org/doi/10.1103/PhysRev.108.1063

[6] F. J. Zerilli, "Effective potential for even-parity regge-wheeler gravitational perturbation equations," *Phys. Rev. Lett.*, vol. 24, pp. 737–738, Mar 1970. [Online]. Available: https://link.aps.org/doi/10.1103/PhysRevLett.24.737

[7] S. Chandrasekhar, *The mathematical theory of black holes.* Oxford University Press, 1992.

[8] Abbott *et al.*, "Observation of gravitational waves from a binary black hole merger," *Phys. Rev. Lett.*, vol. 116, p. 061102, Feb 2016. [Online]. Available: https://link.aps.org/doi/10.1103/PhysRevLett.116.061102

[9] J. Stewart, *The Newman-Penrose formalism*, ser. Cambridge Monographs on Mathematical Physics. Cambridge University Press, 1991, p. 216–221.

[10] W. H. Press and S. A. Teukolsky, "Perturbations of a Rotating Black Hole. II. Dynamical Stability of the Kerr Metric," *Astrophys. J.*, vol. 185, pp. 649–674, 1973.

[11] S. A. Teukolsky, "Perturbations of a Rotating Black Hole. I. Fundamental Equations for Gravitational, Electromagnetic, and Neutrino-Field Perturbations," , vol. 185, pp. 635–648, Oct. 1973.

[12] K. Glampedakis, G. Pappas, H. O. Silva, and E. Berti, "Post-kerr black hole spectroscopy," *Phys. Rev. D*, vol. 96, p. 064054, Sep 2017. [Online]. Available: https://link.aps.org/doi/10.1103/PhysRevD.96.064054

[13] E. Berti, V. Cardoso, and C. M. Will, "Gravitational-wave spectroscopy of massive black holes with the space interferometer lisa," *Phys. Rev. D*, vol. 73, p. 064030, Mar 2006. [Online]. Available: https://link.aps.org/doi/10.1103/PhysRevD.73.064030

[14] T. Johannsen and D. Psaltis, "Metric for rapidly spinning black holes suitable for strong-field tests of the no-hair theorem," *Phys. Rev. D*, vol. 83, p. 124015, Jun 2011. [Online]. Available: https://link.aps.org/doi/10.1103/PhysRevD.83.124015

[15] E. Newman and R. Penrose, "An Approach to gravitational radiation by a method of spin coefficients," *J. Math. Phys.*, vol. 3, pp. 566–578, 1962.

[16] J. G. Williams, S. G. Turyshev, and D. H. Boggs, "Progress in lunar laser ranging tests of relativistic gravity," *Phys. Rev. Lett.*, vol. 93, p. 261101, Dec 2004. [Online]. Available: https://link.aps.org/doi/10.1103/PhysRevLett.93.261101

[17] L. Kong, Z. Li, and C. Bambi, "Constraints on the spacetime geometry around 10 stellar-mass black hole candidates from the disk's thermal spectrum," *Astrophys. J.*, vol. 797, no. 2, p. 78, 2014.

[18] Z. Carson and K. Yagi, "Probing beyond-kerr spacetimes with inspiral-ringdown corrections to gravitational waves," *Phys. Rev. D*, vol. 101, p.

084050, Apr 2020. [Online]. Available: https://link.aps.org/doi/10.1103/PhysRevD.101.084050

[19] Z. Ahmed, "GitHub Profile: zkhatri11," https://github.com/zkhatri11?tab=repositories, 2023.

[20] K. Dey, E. Barausse, and S. Basak, "Measuring deviations from the kerr geometry with black hole ringdown," 2022.

[21] G. Carullo, W. Del Pozzo, and J. Veitch, "Observational black hole spectroscopy: A time-domain multimode analysis of gw150914," *Phys. Rev. D*, vol. 99, p. 123029, Jun 2019. [Online]. Available: https://link.aps.org/doi/10.1103/PhysRevD.99.123029

[22] C. D. Capano, J. Abedi, S. Kastha, A. H. Nitz, J. Westerweck, Y.-F. Wang, M. Cabero, A. B. Nielsen, and B. Krishnan, "Statistical validation of the detection of a sub-dominant quasi-normal mode in gw190521," 2022.

[23] Alex Nitz, *et al.* (2022, Jul.) gwastro/pycbc: v2.0.5 release of pycbc. [Online]. Available: https://doi.org/10.5281/zenodo.6912865

[24] V. Cardoso, M. Kimura, A. Maselli, and L. Senatore, "Black holes in an effective field theory extension of general relativity," *Phys. Rev. Lett.*, vol. 121, p. 251105, Dec 2018. [Online]. Available: https://link.aps.org/doi/10.1103/PhysRevLett.121.251105

[25] P. A. Cano, K. Fransen, T. Hertog, and S. Maenaut, "The universal teukolsky equations and black hole perturbations in higher-derivative gravity," https://arxiv.org/abs/2304.02663, April 2023.

Appendix A

Appendix

A.1 Explicit form of post-Kerr terms

Here we list the numerous terms mentioned in section 3 First we show the Kerr coefficients labelled with a subscript K. R_K, H_K, N_K:

$$R_K = (19M^2 + 26a^2)Mr_K + 3Ma^2(8M^2 + 7a^2) - (54M^4 + 40M^2a^2 - 4a^4)r_K$$

(A.1)

$$H_K = \frac{1}{2}\left(\frac{r_K}{M}\right)^{1/2}(r_K - M)[6\Delta_K h_{rr} - r_K^2\Delta_K h''_{\phi\phi}] - 6r_{ph}(r_K - 2M)h_{\phi\phi}$$
$$\pm r_K\Delta_K W_{t\phi}h'_{t\phi} \mp 2r_K M_{t\phi}[r_K\Delta_K h''_{t\phi} + 6(r_K - 2M)h_{t\phi}]$$
$$+ \left(\frac{r_K}{M}\right)^{1/2}r_K[3K_{tt}h_{tt} - \Delta_K(Q_{tt}h'tt) + r_K J_{tt}h''_{tt}]$$
$$+ r_K\Delta_K\left(\frac{r_K}{M}\right)^{1/2}(2r_K - 5M)h'_{\phi\phi}$$

(A.2)

$$N_K = (Mr_K)^{1/2}(G_{\phi\phi}h''_{\phi\phi} + G_{tt}h''_{tt}$$
$$+ 2Z_{tt}h'_{tt} + 2G_{\phi\phi}h'_{\phi\phi} + 2E_{tt}h_{tt} + 2E_{\phi\phi}h_{\phi\phi} + 6E_{rr}h_{rr})$$
$$\pm M(G_{t\phi}h''_{t\phi} + 4Z_{t\phi}h'_{t\phi} + 8E_{t\phi}h_{t\phi})$$

(A.3)

Now the remaining coefficients $E_{rr}, E_{tt}, E_{t\phi}, E_{\phi\phi}, M_{t\phi}, W_{t\phi}, K_{tt}, Q_{tt}, J_{tt}, S_{tt}$, $S_{t\phi}, S_{\phi\phi}, Z_{tt}, Z_{t\phi}, Z_{\phi\phi}, G_{\phi\phi}, G_{t\phi}$ and G_{tt}:

$$M_{t\phi} = 2r_K^2 - 2Mr_K + a^2 \tag{A.4}$$

$$W_{t\phi} = 13r_K^2 - 33Mr_K + 8a^2 \tag{A.5}$$

$$K_{tt} = -(33M^2 + a^2)r_K^2 + 9(9M^2 - a^2)Mr_K - 38M^2a^2 \tag{A.6}$$

$$Q_{tt} = -21Mr_K^2 + 2(27M^2 - a^2)r_K - 19Ma^2 \tag{A.7}$$

$$J_{tt} = \frac{1}{2}[15Mr_K^2 + (a^2 - 27M^2)r_K + 11Ma^2] \tag{A.8}$$

$$
\begin{aligned}
G_{\phi\phi} = {} & -(351M^6 + a^6 787M^4a^2 + 157M^2a^4)r_K^2 + 12M(133M^4a^2 \\
& + 81M^6 + 3a^4M^2 - a^6)r_K - 48M^2a^2(2a^4 + 16M^2a^2 + 9M^4)
\end{aligned} \tag{A.9}
$$

$$
\begin{aligned}
G_{tt} = {} & -(10935M^8 + 36666M^6a^2 + a^8 + 15160M^4a^4 + 742M^2a^6)r_K^2 \\
& + 6M(2769M^4a^4 - 227M^2a^6 + 5103M^8 + 13527M^6a^2 - 4a^8)r_K \\
& - 24M^2a^2(485M^2a^4 + 567M^6 + 13a^6 + 1581M^4a^2)
\end{aligned} \tag{A.10}
$$

$$
\begin{aligned}
G_{t\pi} = {} & -3M(a^2 + 27M^2)(83a^4 + 262M^2a^2 + 87M^4)r_K^2 + (19683M^8 \\
& - 272M^2a^6 + 46683M^6a^2 + 6941M^4a^4 - 4a^8)r_K \\
& - 12Ma^2(7a^6 + 459M^2a^4 + 729M^6 + 1829M^4a^2)
\end{aligned} \tag{A.11}
$$

$$
\begin{aligned}
Z_{tt} = {} & -M(131a^6 + 6345M^4a^2 + 3379a^4M^2 + 729M^6)r_K^2 \\
& + (2187M^8 - 2a^8 - 361M^2a^6 + 15309M^6a^2 + 4035M^4a^4)r_K \\
& - 4Ma^2(11a^6 + 1737M^4a^2 + 243M^6 + 655a^4M^2)
\end{aligned} \tag{A.12}
$$

$$
\begin{aligned}
Z_{t\phi} = {} & -(1917M^4a^2 + 845a^4M^2 + 19a^6 + 234M^6)r_K^2 \\
& + M(847a^4M^2 - 91a^6 + 729M^6 + 4563M^4a^2)r_K - 4a^2(a^6 + 81M^6 \\
& + 519M^4a^2 + 155a^4M^2)
\end{aligned} \tag{A.13}
$$

$$E_{rr} = (4a^6 + 154M^2a^4 + 135M^6 + 436M^4a^2)r_K^2$$
$$- 2M(189M^6 - 8a^6 + 70M^2a^4 + 478M^4a^2)r_K$$
$$+ a^2(112M^2a^2 + 448M^4a^2 + a^6 + 168M^6) \tag{A.14}$$

$$E_{tt} = -(549M^4a^2 - a^6 + 1377M^6 - 161a^4M^2)r_K^2$$
$$+ 3M(15M^2 - a^2)(8M^2a^2 + 81M^4 - 5a^4)r_K$$
$$- 4M^2a^2(405M^4 - 29a^4 + 65M^2a^2) \tag{A.15}$$

$$E_{\phi\phi} = -(39M^4 - a^4 - 2M^2a^2)r_K^2 + 3M(33M^4 + a^4 - 10M^2a^2)r_K$$
$$- 4M^2a^2(11M^2 - 2a^2) \tag{A.16}$$

$$E_{t\phi} = -4M(54M^4 + 14M^2a^2 - 5a^4)r_K^2 + (567M^6 - 45M^4a^2$$
$$- 19a^4M6 + a^6)r_K - 12Ma^2(21M^4 + M^2a^2 - a^4) \tag{A.17}$$

$$S_{tt} = 9(3673M^4a^2 + 1053M^6 + 947a^4M^2 + 11a^6)r_K^2 - M(4151a^4M^2$$
$$+ 71901M^4a^2 + 26973M^6 - 713a^6)r_K + 4a^2(8409M^4a^2 + 2997M^6$$
$$+ 1379a^4M^2 + 4a^6) \tag{A.18}$$

$$S_{\phi\phi} = 3(226M^2a^2 + 105M^4 + 17a^4)r_K^2 - M(1298a^2M^2$$
$$+ 891M^4 - 101a^4)r_K + 4a^2(158M^2a^2 + 99M^4 + 4a^4) \tag{A.19}$$

$$S_{t\phi} = (r_K + 3M)(Mr_K)^{-1/2}(M(2770M^2a^2 + 999M^4 + 407a^4))r_K^2$$
$$- (2835M^6 + 5706M^4a^2 - 173a^4M^2 - 16a^6)r_K$$
$$+ 12Ma^2(226M^2a^2 + 105M^4 + 17a^2) \tag{A.20}$$

A.2 Post-Kerr offset function

The offset function β^K we introduced in section 3.1 ensures that we are within reasonable bounds for using a non-Kerr QNM template.

$\beta^K(a)$ is used as a numerical tool to fit tabulated Kerr QNM data [13] inspired by the classic interatomic Buckingham potential.
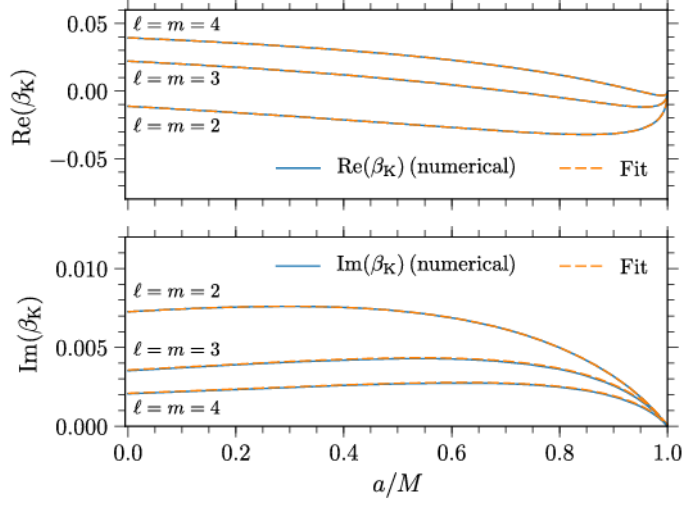
Figure A.1: Fitting the real and imaginary parts of β^k numerically for $l = m = 2, 3, 4$. The trend is similar for higher modes.

This Buckingham potential takes the form:

$$f(x) = a_1 + a_2 e^{-a_3(1-x)^{a_4}} - \frac{1}{a_5 + (1-x)^{a_6}} \tag{A.21}$$

$\ell = m$	a_1	a_2	a_3	a_4	a_5	a_6	max err. $[10^{-2}]$
2	0.1282(0.1381)	0.4178(0.3131)	0.6711(0.5531)	0.5037(0.8492)	1.8331(2.2159)	0.7596(0.8544)	0.023(0.004)
3	0.1801(0.1590)	0.5007(0.3706)	0.7064(0.6643)	0.5704(0.6460)	1.4690(1.8889)	0.7302(0.6676)	0.005(0.008)
4	0.1974(0.1575)	0.4982(0.3478)	0.6808(0.6577)	0.5958(0.5840)	1.4380(1.9799)	0.7102(0.6032)	0.011(0.009)
5	0.2083(0.1225)	0.4762(0.1993)	0.6524(0.4855)	0.6167(0.6313)	1.4615(3.1018)	0.6937(0.6150)	0.016(1.335)
6	0.2167(0.1280)	0.4458(0.1947)	0.6235(0.5081)	0.6373(0.6556)	1.5103(3.0960)	0.6791(0.6434)	0.021(0.665)
7	0.2234(−15.333)	0.4116(15.482)	0.5933(0.0011)	0.6576(0.3347)	1.5762(6.6258)	0.6638(0.2974)	0.025(0.874)

Figure A.2: Fitting coefficients a_i of the Buckingham potential for different $l = m$ modes

A.3 JP Expansion Coefficients

The JP deviation terms in equations 3.29 and 3.30 are written in terms of the coefficients C_-, C_+ and C_0 as follows:

$$\delta r_1 = -\frac{b_K M C_+^5}{18 C_-^2 C_0} \tag{A.22}$$

$$\delta b_1 = \frac{54 M^2 C_- C_+^4 + C_+^7}{54 C_-^2 C_0} \tag{A.23}$$

$$\begin{aligned}
\delta\gamma_1 = \gamma_K^3 \frac{27 M^2 C_-^2 + a(a - 2b_K)C_+^2}{2 C_+^5 C_0 (3 M^2 (5a - b_K)C_- + a^2 C_+^2)^3} &[a^3(4a^2 - ab_K - 6b_K^2)C_+^{10} \\
&+ 729 M^6 C_-^3 (364 a^4 - 227 a^3 b_K - 201 a^2 b_K^2 - 29 a b_K^3 + 13 b_K^4)C_+^2 \\
&+ 27 M^4 C_-^2 (2a + b_K)(319 a^4 - 174 a^3 b_K - 216 a^2 b_K^2 - 38 a b_K^3 + 9 b_K^4)C_+^4 \\
&+ a M^2 C_- (454 a^4 - 133 a^3 b_K - 366 a^2 b_K^2 - 182 a b_K^3 + 2 b_K^4)C_+^7 \\
&+ 78732 M^8 C_-^5 (5a - b_K)(4a + b_K)]
\end{aligned} \tag{A.24}$$

The coefficients are defined as:

$$C_+ \equiv a + b_K \tag{A.25}$$

$$C_- \equiv a - b_K \tag{A.26}$$

$$C_0 \equiv (4a + b_K) 27 M^2 C_- + 2 C_+^4 \tag{A.27}$$

University
of Stavanger

4036 Stavanger
Tel: +47 51 83 10 00
E-mail: post@uis.no
www.uis.no